QUALITATIVE CONDITION MONITORING OF RAIL STEEL

by

JESSICA ELIZABETH PAYNE

A thesis submitted to the University of Birmingham for the degree of

MSc BY RESEARCH

UNIVERSITY OF BIRMINGHAM

School of Metallurgy and Materials
College of Engineering and Physical Sciences
University of Birmingham

July 2022

Abstract

To meet the growing demand for rail travel and keep customers satisfied, disruption to services must be minimised. Currently used rail inspection techniques require rail access which prevents 24h operation of rolling stock. The replacement of these disruptive techniques with passive remote monitoring methods can provide economic benefits to those who use and supply rail travel whilst improving customer satisfaction.

Acoustic Emission (AE) is an inspection technique that can passively and continuously collect health degradation data while attached to the surface of a material. It has previously been identified as capable of detecting and locating growing defects within rails and crossings and recent work has focused on its use to quantify fatigue cracks as they propagate. Active inspection can be used to quantify defects that have previously propagated whilst AE testing can provide information on damage as it occurs. To predict future health degradation, it is necessary to use modelling. Recent work regarding the modelling of rails have included improvements to the accuracy of modelling the material behaviour whilst keeping the processing effort reasonably low (due to the large number of cycles that rails operate over). Links have also started to be made between Finite Element Analysis (FEA) and AE, with a goal of aiding AE data interpretation.

A three-point bending fatigue test was performed on ten notched and pre-cracked samples of cast manganese steel (otherwise known as Hadfield steel). AE was measured by two sensors, the outputs of which were parametric and waveform analysis respectively. The crack length was measured throughout the test using Direct Current Potential Drop (DCPD). A similar experiment was performed in recent work on R260 steel samples; data from the experiment was further analysed in this work. The waveform AE data and recorded force for each event was used to calibrate the parametric AE data to the true frequency so that a more accurate cycle number for each event was used and the cycle stage at which hits were measured could be analysed. For the Hadfield steel, the parametric AE data was compared to the crack growth rate to attempt quantification using the AE count rate.

Finite Element Analysis was also performed to simulate a crack growing through an inclusion in R260 steel and investigate the resultant energy release for comparison with previous work in the literature that related the location of an inclusion along the surface of a fatigue crack to the time at which a significant step in cumulative AE energy was measured.

In both Hadfield steel and R260 steel, AE events that remained after filtering were determined to primarily be generated by crack

propagation and friction as the crack opened and closed. Events that were measured during loading (due to crack propagation and friction of surfaces during crack opening) occurred earlier in the cycle as the crack grew, whilst events that were measured during unloading (due to friction during crack closure) appeared to occur at a consistent cycle stage.

Contrary to what was previously observed for R260 steel samples, the Hadfield steel samples showed no relationship between the count rates or energy rates and the stress intensity factor range (ΔK). As a result, no link could be made between the measured AE parameters and the crack growth. Therefore, crack length quantification using AE could not be achieved for the Hadfield steel samples.

The FEA inclusion model showed that soft MnS inclusions can cause fast crack propagation and a related step in energy released. This supported the suggestion in previous work that an observed step in cumulative AE energy was a result of fast crack propagation caused by an inclusion.

Finally, a digital twin for rail is conceptualised which uses inputs of measured mechanical loads and AE for a section of track to reproduce defect growth and material behaviour. Implementation of an inspection technology such as this, if accurate, would vastly reduce inspection and maintenance costs whilst raising confidence in rail health.

Acknowledgements

I am extremely grateful to Dr Mayorkinos Papaelias for the guidance, feedback, and knowledge he provided along with the valuable opportunity to work under his supervision. I would also like extend my deepest gratitude to Dr Valter Jantara Junior for all of the advice, insights, and words of encouragement he offered throughout my time as a post-graduate researcher. I am greatly appreciative of the University of Birmingham, the EPSRC and the European Commission for the provision of funding during this project.

Many thanks to Richard Culwick who prepared the samples and assisted with the experimental work. Thanks also to Dr Timothy Doel who operated the fatigue testing machinery. I am also grateful to the School of Metallurgy and Materials for access to the testing facilities. Thanks also to Network rail for the advice and technical support provided.

Finally, I would like to thank my family and friends for their support. In particular I would like to express my deepest appreciation to my fiancé and best friend James Brady, without whom I would have been unable to get this far.

Contents

List of Figures

List of Tables

Nomenclature

Abbreviations

AE	Acoustic Emission
ALLDMD	Energy release related to crack growth (ABAQUS)
ALLPD	Energy release related to plasticity (ABAQUS)
DCPD	Direct Current Potential Drop
ECT	Eddy Current Testing
FEA	Finite Element Analysis
MFL	Magnetic Flux Leakage
NDT	Non-Destructive Testing
RCF	Rolling Contact Fatigue
RMS	Root Mean Square
TPB	Three-Point Bending
UT	Ultrasonic Testing
XFEM	Extended Finite Element Method

Material Models

AF	Armstrong-Frederick
AKO	Abdel-Karem-Ohno
BC	Burlet-Cailletaud
CL	Chaboche and Lemaitre
OW	Ohno-Wang

Symbols

$\beta_0, \beta_1, \gamma_0, \gamma_1, \delta_0, \delta_1, \delta_2, \epsilon_0, \epsilon_1, \epsilon_2, B_0, B_1, \Gamma_0, \Gamma_1, m, n, D_1, D_2, D_3, C$	Constants
ΔK	Stress intensity factor range

$\dot{\epsilon_0}$	Reference strain rate
$\dot{\epsilon}$	Strain rate
ϵ_{pl}	Plastic strain
ϵ	Strain
σ_y	Yield strength
σ_{eq}	Equivalent stress
a	Crack length
$a.u.$	Arbitrary units
a_0	Initial crack length
B	Sample thickness
C_c	Cumulative AE counts from crack closure
C_p	Cumulative AE counts from crack propagation
E_c	Cumulative AE energy from crack closure
E_f	Cumulative AE energy at failure
e_i	AE Event energy
E_p	Cumulative AE energy from crack propagation
F	Frequency
G_{IC}	Fracture Energy
K_{IC}	Fracture toughness
K_{Max}	Maximum stress intensity factor
K_{Min}	Minimum stress intensity factor
P	Force
P_{Max}	Maximum force
P_{Min}	Minimum force
s	Distance from the AE source to the AE sensor

T^*	Temperature function
T_T	Time for an AE signal to reach the AE sensor
U	Voltage
U_0	Initial voltage
V	Speed of AE wave propagation
W	Sample width
y	Half DCPD probe distance
a_f	Crack length at failure
E	Young's modulus
N	Cycles
N_f	Cycles to failure

1 INTRODUCTION

Due to a rise in global population and increasing environmental awareness, there is growing demand for environmentally benign public transport such as rail travel. According to the National Travel Survey, the average miles over which a citizen of England travelled by rail in a year rose by 43% between 2002 and 2019 (before dropping in 2020 due to the Coronavirus pandemic) which was a larger increase than any other method of public transport as shown in Figure 1 [1].

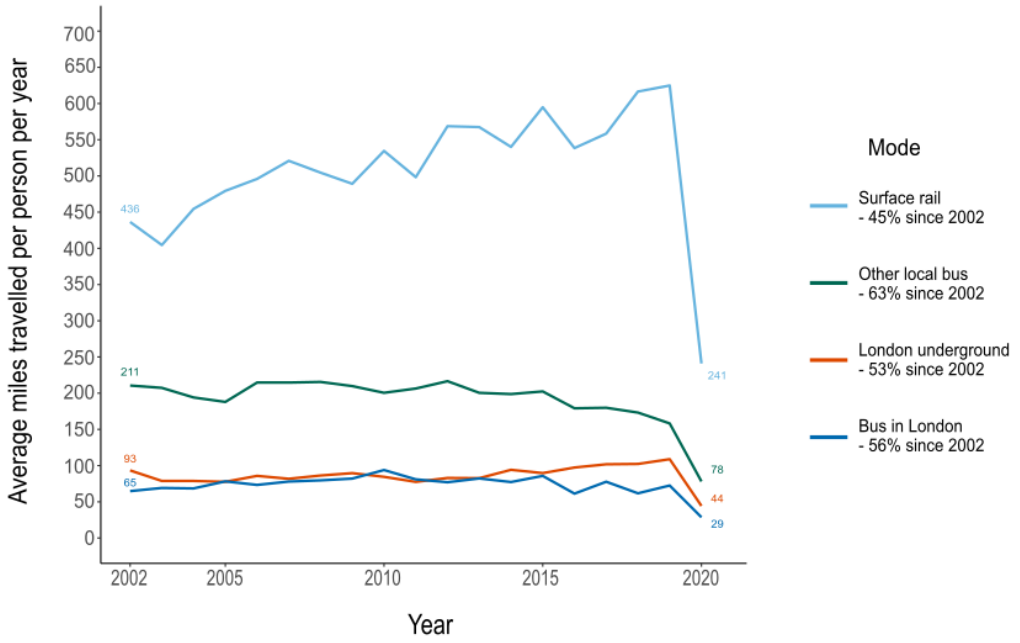

Figure 1: Miles travelled by the average person using different types of public transport in England over a year (self reported) [1].

As the number of rail journeys increases, the demand for 24-hour rail network access will become more imperative. At the moment, trains do not run overnight regularly to enable inspection and maintenance activities to be performed. To minimise disruption and ensure that the demand can be met,

more sophisticated solutions are required for inspection and maintenance of rail infrastructures that ensures the safe and reliable operation of passenger and freight trains.

In the general case for a given component, the prioritisation and performance of maintenance activities are influenced by many different factors, such as [26]:

- Frequency of failure
- Predictability of degradation and failure
- How easy and similar maintenance activities are
- The likelihood and impact of manufacturing defects
- Risks linked to failure
- Economic and societal impact of failure

In the case of rails, failure frequency due to wear and fatigue is currently kept at a very low level (it should be eliminated all together in an efficient high-speed network). Prediction of rail failure is very challenging due to the variability of operational conditions and stochastic loads that are involved. Also, the effects of potential interventions due to maintenance and repairs cannot be ignored in the accurate estimation of the remaining lifetime of rail infrastructure. The ease of repairs and replacement depends on the complexity of the track in a particular location, e.g. presence of embankments, wet beds, etc..

Unexpected rail failures can have very serious consequences since they can lead to severe train derailments which can result in casualties, environmental damage, economic impact and loss of confidence in rail transport by the public and businesses. Emergency maintenance and repairs can be performed to avoid the undesirable effects of potential derailments but can cause cancellations, disruption and delays. The result is not only higher operational costs and loss of revenue, but also inconvenience to consumers who may be influenced to preferentially travel by other modes of public transport in the future.

The safety risks and economic impact associated with rail failure means that it is an unacceptable outcome. Maintenance must therefore be preventative as a minimum requirement. Maintenance activities must be effective and cost-efficient, leading to improved reliability and safety of long-term rail operations. The ideal maintenance solution is one where it is known exactly when a component will require intervention either in the form of repair or replacement. However, it can be difficult to identify that time-frame accurately and safety critical applications such as rail infrastructure require an element of acceptable confidence in any estimates made. This means that components should be repaired or replaced with sufficient time left before failure can actually become possible. It should never be allowed that any critical structural component of the rail infrastructure sustains damage which is sufficient to make final failure imminently possible.

In reality, there are several different approaches to inspection and maintenance strategies that have trade-offs with respect to the overall cost of inspection, cost of maintenance, efficiency, accuracy and reliability. These

approaches are outlined in Table 1. Current maintenance of rails is typically performed on a planned basis. It is both corrective and preventative, although performed in a very conservative way due to its safety-critical nature. At the same time, inspection is active and requires rail access. The implementation of predictive maintenance supported by passive inspection methods would improve efficiency, lower costs, and minimise disruption, making it a very desirable solution. On the other hand, the effectiveness of predictive maintenance can be significantly limited by underestimates or overestimates due to uncertainties associated with inspection and remaining lifetime analysis.

Table 1: Types of preventative maintenance, summarised from [16].

	Summary	**Advantages**	**Disadvantages**
Planned maintenance	Maintenance is performed at pre-defined intervals	Simple	Components may be replaced earlier than needed
Condition-based maintenance	Maintenance is performed if a health threshold is passed by the component	Components can be used for longer	High effort required for monitoring
Predictive maintenance	The time until failure is predicted and maintenance is planned accordingly	Early intervention can expand component life and lower costs	Higher uncertainties than condition-based monitoring

Acoustic Emission (AE) is a passive, continuous monitoring technique that can be used to monitor rail infrastructural structural degradation in

real-time without disrupting operation and leading to optimization of the availability of rail tracks.

The present study focused on the development of an effective AE analysis methodology as a tool for detecting, locating, and quantifying health degradation within rails and crossings. This was investigated both physically, with experimental fatigue crack growth in three-point bending monitored with AE, and theoretically with Finite Element Analysis (FEA) of a sample containing a soft sulphide inclusion. An aim for such analyses is to facilitate the creation of an operational digital twin. The successful application of such a model would reduce maintenance costs by allowing for early intervention in defects (by way of predictive maintenance) as well as increasing confidence in the estimation of the remaining lifetime of key rail infrastructure structural assets.

2 LITERATURE REVIEW

2.1 Rail Materials and Application

In a broad sense, the role of a rail is to provide a surface which supports and guides rolling stock. Rails must therefore have a surface that provides sufficient traction and a structure that can support the high loads that are exerted. The geometry of a rail as well as the forces exerted on it by a wheel are shown in Figure 2.

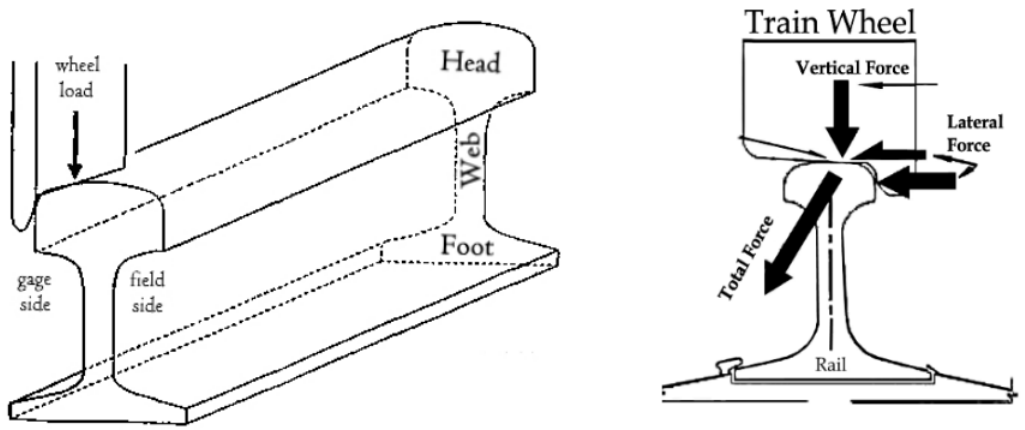

Figure 2: Left: Labelled rail diagram adapted from [2]. Right: Force at the contact point between the rail and a wheel adapted from [3].

Rails are attached by fasteners to sleepers (typically concrete, although in older lines sleepers may be made of wood and less often of steel) which are placed on top of ballast as shown in Figure 3. Ballast forms the foundation of the track and is formed of stones of different shapes and sizes. The role of the ballast is to secure the sleepers whilst allowing any water to drain without accumulating in the track structure as the occurrence of wet beds can result in lower track stiffness.

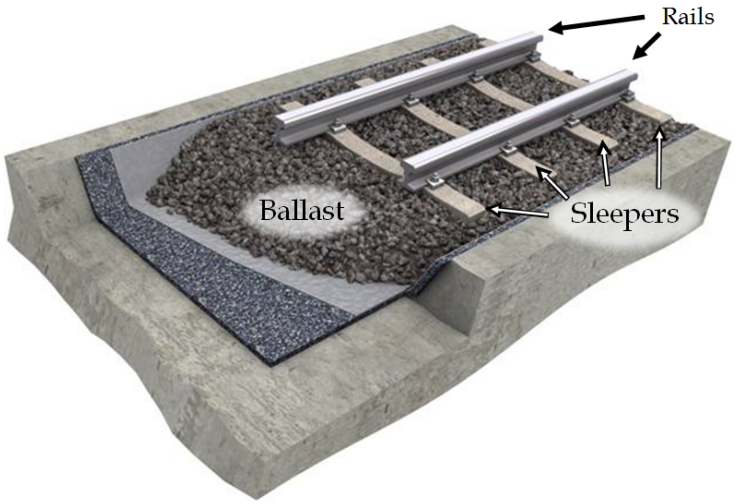

Figure 3: Labelled diagram of rail attachment. Adapted from [4].

Acording to Network Rail, the UK sees an average of around 100 rail failures a year [27]. Most of these failures are fixed before causing an accident. However, there have been a few cases in the past where serious incidents have occurred due to rail track failure. The most notable of these in the UK was the Hatfield crash on Sunday the 17^{th} of October 2000 which resulted in 4 deaths and over 70 people injured [28]. The cost for repair of the track was in the tens of millions [29]. Aside from the immediate high cost of life and health of many passengers and the repair costs, there were also severe ramifications within the rail industry. This included major disruption to travel as speed restrictions were put in place as health checks were performed on other areas of the rail, as well as a loss of consumer confidence in rail travel [30]. It was a few years before business returned to the state it had been before the crash [30].

2.1.1 Rail Manufacture and Microstructure

Rails are typically made of pearlitic grades of steel although bainitic grades are also used in areas of high expected wear [17]. Some examples of rail steels along with their compositions and properties can be seen in Table 2.

Table 2: The composition and properties of a some commonly used rail steels [17]. The remainder of the composition is iron.

Rail		Structure	Content of elements, wt.%				Mechanical properties		
			C	Si	Mn	Cr	$\sigma_{r\,min}$, MPa	δ_{min}, %	Hardness, *BNH*
Dobain 340	(*1*)	Bainite	0.76 – 0.84	0.20 – 0.35	0.80 – 0.90	0.40 – 0.55	1100	11	340 – 380
Dobain 380	(*2*)		0.76 – 0.84	0.20 – 0.35	0.80 – 0.90	0.40 – 0.55	1250	10	380 – 420
Dobain 430	(*3*)		0.76 – 0.84	0.20 – 0.35	0.80 – 0.90	0.40 – 0.55	1400	9	> 430
400UHC	(*4*)	High-quality pearlite	0.90 – 0.95	0.20 – 0.35	1.20 – 1.30	0.25 – 0.30	1240	9	> 400
380UHC	(*5*)		0.90 – 0.95	0.20 – 0.35	1.20 – 1.30	0.25 – 0.30	1200	9	> 380
370LHT	(*6*)		0.70 – 0.82	0.40 – 1.00	0.70 – 1.10	0.40 – 0.70	1175	9	> 370
R350HT	(*7*)	Standard pearlite	0.72 – 080	0.15 – 0.58	0.70 – 1.20	≤ 0.15	1175	9	350 – 390
R260	(*8*)		0.62 – 0.80	0.15 – 0.58	0.70 – 1.20	≤ 0.15	880	10	260 – 300
R220	(*9*)		0.50 – 0.60	0.20 – 0.60	1.00 – 1.25	≤ 0.15	770	12	220 – 260

During manufacture, most rails are initially continuously cast, rolled several times until the desired dimensions are achieved, and subsequently cut into the 12-metre long sections. When they are installed on the track they are flash-butt welded to form a continuous welded track. Joints are typically found in older lines and in stations where speeds are lower. Inspection is performed on the rails after the manufacturing process to check for conformity to the required standards with regards to inclusions and any other physical defects.

Due to the rolling stages of manufacture, there are internal residual stresses in the longitudinal versus transversal directions [5, 20]. Residual stresses as the result of different manufacturing stages can be observed in [5]. Residual stresses near the rail head surface can be altered due to wear

and plastic deformation from axle loads while the rails are in-service. Figure 4 shows the internal stresses (produced using neutron diffraction) of a newly manufactured rail [5]. It can be observed that residual tensile stresses reach high values in the transverse and longitudinal planes, while compressive stresses reach high values in the transverse and vertical planes. The compressive stress at the surface of the rail is thought to offer some protection against fatigue whilst the tensile layer is thought to potentially allow faster growth if reached by the crack, or if a crack nucleates within this region [31].

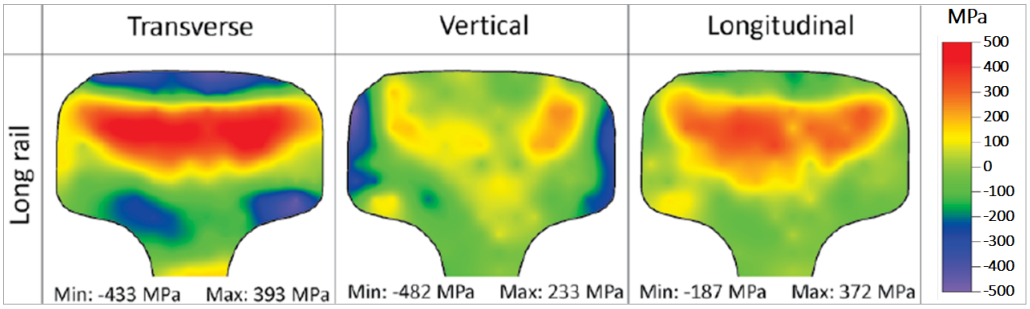

Figure 4: Residual stresses in a rail in the transverse, vertical and longitudinal directions. Reformatted from reference [5].

The fracture toughness, yield stress, ductility, wear resistance and hardness of pearlitic rail steel grades, such as R260, is strongly related to the pearlite interlamellar spacing, with smaller spacing resulting in a harder material [32, 33]. Head-hardening is desirable in rails in order to increase the resistance to rolling contact fatigue and wear and can be achieved by fast-cooling the head after hot-rolling, or by heat treating the head after manufacturing [34, 35]. The result is an inhomogeneous microstructure where the interlamellar spacing increases with the distance from the head surface.

Virgin rails therefore show varied material properties along the vertical

and transverse axes. This is further compounded by work hardening as the rails are stochastically loaded by the wheels of rolling stock. It has been observed that the hardening behaviour of head-hardened pearlitic steel under cyclic load varies along the material depth from the surface of the head. As the depth from the head surface increases and the hardness of the material decreases its plastic response goes from showing hardening behaviour to exhibiting softening behaviour for the same load-case [6, 36–38]. The effect is shown in Figure 5.

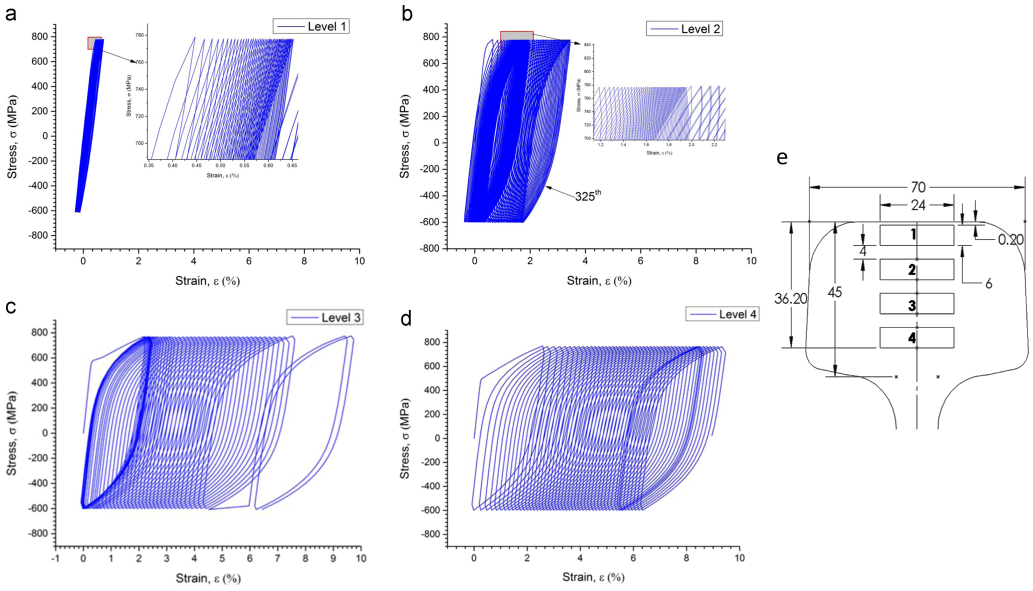

Figure 5: Hardening behaviour exhibited in a head-hardened pearlitic steel (AS60 HH) removed from different depths from the surface of the rail. a-d) Cyclic stress-strain behaviour of samples 1-4 respectively, e) positions of samples in rail prior to extraction [6].

For rail crossings (otherwise known as turnout frogs), as shown in Figure 6, cast manganese steel (also known as Hadfield steel) is used. Its composition is given in Table 3. The high content of manganese allows the alloy to have a face-centred cubic austenitic structure by stabilising the austenite phase

[33]. It has a high propensity to work harden which results in superior hardness, wear resistance, and fracture toughness which is ideal for coping with the increased demands such as frequent impact loads [33, 39]. These properties also make the material difficult to machine, hence, crossings are manufactured by casting. As they are not rolled, they are more homogeneous than standard rail sections after initial manufacture. However, after work hardening (through explosive hardening before operation and/or the impact of rolling stock during operation) crossings have properties that reduce with the depth from the head surface [40–43].

Figure 6: An example of a rail turnout where Hadfield steel is typically used [7].

Inclusions in Rail Steel

During the manufacture of pearlite rail steel, inclusions are not completely avoidable. These inclusions can be hard and brittle (e.g. Fe_3C, Al_2O_3) or soft

Table 3: Typical composition of Hadfield steel used in rail crossings [18]. Values are given as a percentage, with the remainder of the composition being iron.

C	Mn	Si	Cr	Mo	V	Al	P	S
1.05-1.15	11.5-14.0	≤ 0.65	≤ 0.5	≤ 0.5	≤ 0.5	≤ 0.05	≤ 0.03	≤ 0.03

and ductile (e.g. MnS). Hard inclusions resist deformation during manufacture. If they are allowed to form or added to the steel from contamination, then the steel may end up containing large, irregular inclusions with poor deformability which can hinder fatigue resistance by causing stress concentrations leading to early crack initiation and subsequent propagation [44, 45]. A way in which their prevalence in rail steel has been reduced is by performing de-oxygenation using Silicon atoms rather than Aluminium. To reduce the impact of hard inclusions, manufacturing and testing has improved in an effort to reduce their occurrence. This is done by careful refining in the initial stages of manufacture (such as vacuum degassing) and inspection to ensure that where present, hard inclusions are small and distributed [33].

In contrast, soft inclusions are deformed as the rails undergo rolling during manufacture. They are therefore typically long and thin in appearance. Manganese sulphide is the most common soft inclusion in rail steel and in some ways its presence is beneficial. MnS inclusions can slow grain growth, improving the properties of the matrix, improve machinability of the metal, and also help to prevent hydrogen-induced fractures by trapping hydrogen atoms [22]. However, these benefits are outweighed by the detrimental effect they can have. Their deformability results in subsurface cracks and an in-

creased wear rate [46]. Risks associated with MnS inclusions in rail steel can be reduced through treatment with elements such as Calcium or titanium which can cause preferential inclusions to form, resulting in better performance [22, 47]. Increasing the cooling rate has also been found to decrease the final size of the MnS inclusions [47].

Inclusions can also occur in Hadfield rail steel used for crossings. These are typically complex carbides at grain boundaries which can reduce the ductility of the steel as well as significantly reducing its impact strength [39]. Such inclusions can be reduced or removed through optimised heat treatment [39].

2.1.2 Rail Conditions and Failure

Loading Conditions

The loads experienced by rails are often significantly large, but also stochastic. Not only does loading depend upon the axle loads of the vehicle travelling over it, but also factors such as wheel health. If a wheel has a flat, impact loading will occur as it travels along a rail. In a FEA (Finite Element Analysis) study by Bian et al. it was found that a 50 mm flat could result in a periodic force of almost three times the magnitude of that caused by a healthy wheel [48]. It can therefore be complex to predict the stresses that a rail will experience during its life.

Rail Degradation

The high local stresses exerted on the rail through its contact with the wheel often exceed the plastic shakedown limit or the ratcheting threshold. Ratcheting is the accumulation of plastic deformation over time and occurs when this threshold is exceeded. When the ratcheting strain reaches ductility, local material failure will occur in the form of wear or Rolling Contact Fatigue (RCF) initiation (as micro-cracks and voids) [49]. Initiated micro-cracks can grow upwards, connecting to a network of other small cracks and causing material loss through pitting or spalling; or downwards resulting in a growing fatigue crack that can eventually lead to fracture [50–52].

Wear is the removal of material at the surface of a component. It is caused by factors such as abrasion caused by wheels during standard use as well as slipping of wheels during braking. On a curved piece of track, side wear can occur due to the wheels getting into heavy contact with the inner side of the outer rail as the rolling stock's direction of travel is forcibly changed. The result of excessive wear in rails and crossings includes alteration of the track geometry (e.g. the rail head or crossing nose) which can lead to a change in force distribution on the surface as well as the train wheel altering adhesion and possibly leading to derailment even when no rail breakage has occurred [35].

RCF is a mechanism by which cracks can be initiated and grow in the rail head. RCF crack growth rate is in competition with wear rate as shown in Figure 7. Where a rail has a higher wear rate than crack growth rate, initiated cracks will be worn away before they can propagate. On the other

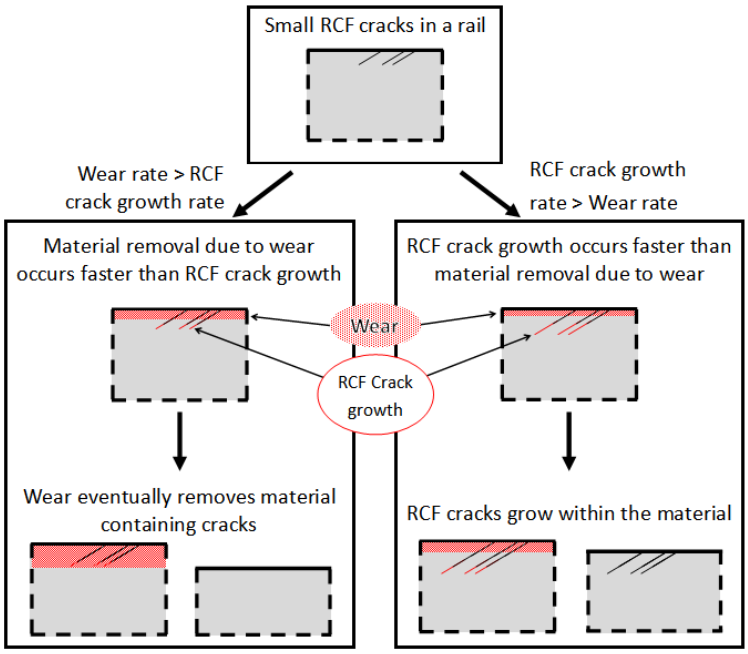

Figure 7: An illustration of the competitive progression of RCF crack growth and wear.

hand, if the crack growth rate surpasses the wear rate then the crack will continue to propagate, potentially to rail failure if it is not detected in time. In moderation, wear can therefore increase rail life although it can be its ultimate limiting factor since when it reaches a predetermined dimensional threshold the rail needs to be replaced [53].

There are thought to be multiple ways in which a crack can initiate in pearlitic rail steel. Work by Garnham et al. has indicated that crack initiation in pearlitic steel can occur at the interface of pearlite and pro-eutectoid ferrite as a result of strain partitioning [54]. It is thought to be for this reason that RCF cracks initiate faster when there is a larger amount of pro-eutectoid ferrite present in the rail steel. In Hadfield steel, crack initiation is thought to occurs due to the growth and combination of voids and to have no relation

to the austenite grain crystal structure [55].

Crack initiation has also been linked to inclusions. The difference in material properties between the matrix and a hard inclusion can cause local failure due to issues such as stress concentrations and debonding (e.g due to different heat expansion coefficients) [44, 45]. Soft inclusions can also act as initiation sites if they are flattened into a disc as this can create a plane of weakness within which cracks or voids can initiate [33].

The direction of crack growth depends on the microstructure as the crack tip will grow in the path that takes the least amount of energy which is affected by material inhomogeneity and residual stresses in the rail [56, 57]. Other factors that affect the growth direction include crack length and angle, presence of liquid, and loading direction [51, 58]. Although the microstructures and deformation of rails and crossings are very different, it has been observed that the morphologies of cracks that propagate within them due to RCF are similar [57].

Failure can be accelerated due to the variability of the rail's hardening behaviour over its depth. Figure 5 shows the change in hardening over the depth of a pearlitic rail steel. When connected as part of a rail, some areas work harden while others soften instead. This effect can become more pronounced as more cycles are applied, resulting in soft sub-surface areas over time. If this soft layer becomes exposed due to wear and grinding, damage may occur at an accelerated rate [6, 36].

Environmental Conditions

Rail behaviour is impacted by temperature. In high temperatures rails will expand and might buckle as demonstrated in Figure 8. Buckling is dangerous as it can cause the derailment of rolling stock. For use in the UK, rails are pre-stressed to have a stress-free temperature of 27 ^{o}C to match the average temperature during the summer months to reduce this risk. However, temperatures on the rail can exceed air temperatures by 20^{o}C meaning that buckling can still occur. The high stress-free temperature also means that for the majority of the year, when temperatures are lower, rails have residual tensile stresses [59].

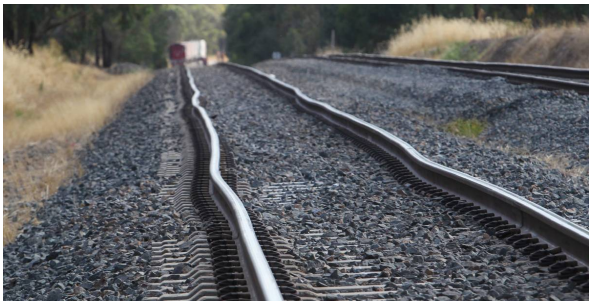

Figure 8: Buckling in a rail [8].

The environmental exposure of rails means that they will often encounter liquid (rain water). As previously mentioned, if wet beds form the stiffness of the rail will decrease although this can typically be avoided by using ballast. Fluid can also penetrate any surface-breaking cracks. This is believed to influence crack growth through friction reduction, increased pressure on crack faces, and by causing hydrostatic pressure at the crack tip through fluid entrapment [51]. The latter is the case where fluid is trapped near the crack tip as the crack is closed by a passing wheel (see Figure 9). The pressure

that is transferred to the liquid as a load is applied, the crack is closed at the surface and the rail is compressed combined with the incompressibility of water results in opening stresses being applied to the crack faces. Wet cracks are theorised to grow in a stable and transverse fashion for this reason. Conversely, dry cracks appear to branch although they can be reverted to a singular fatigue crack in the right conditions (e.g. if a high braking force is applied by a wheel) [51].

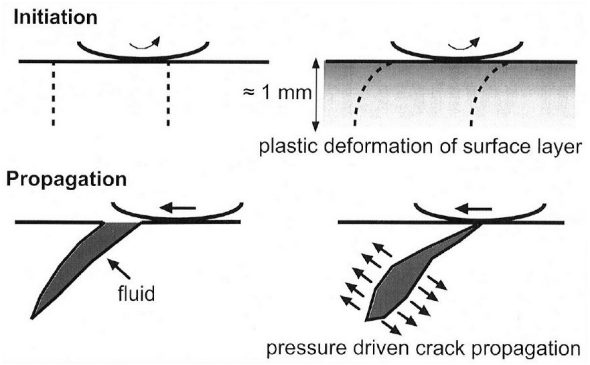

Figure 9: A two-dimensional demonstration of the theory behind fluid entrapment crack propagation [9].

However, fluid entrapment crack propagation theory in rails is challenged by Garnham et al. who highlight the typically long and branching nature of RCF cracks which may be expected to allow fluid to escape, thus preventing the increase in fluid pressure and corresponding opening stress [60]. Nevertheless, the presence of liquid is known to impact crack growth [51, 54, 60].

2.1.3 Rail Inspection

Inspection methods used on rails are typically active and often require rail closure. Multiple types of test are required to ensure that both internal and external defects are detected in each of the head, web and foot of the rail (see

Figure 2). Typical non-destructive test methods (NDT) used include visual inspection, ultrasonic testing (UT), magnetic flux leakage (MFL), and eddy current testing (ECT). These inspection techniques are carried out using test trains, hi-rail vehicles and rail walking sticks. The results of inspection are the detection, location and quantification of the majority of defects including cracks, spalling and corrosion. Often the accuracy of results has an inverse relationship with the speed at which the inspection is performed [61, 62].

In the ideal scenario, rails would be continuously and accurately monitored without causing any disruption (outside of corrective maintenance and replacement). This can be achieved through passive systems which stay on the rail and monitor its health over a sustained period of time. Acoustic emission monitoring is an example of passive inspection which can remotely provide data on occurring deformation, and is the primary focus of this thesis as a solution to rail inspection.

The potential economic benefits of constant, accurate, and passive low cost monitoring are significant. A way this could be achieved is through the use of acoustic emission which will be discussed in the next chapter.

2.2 Acoustic Emission

2.2.1 Basics of Acoustic Emission Monitoring

Acoustic Emission (AE) is defined as the release of elastic transient waves in a solid as a mode of energy dissipation due to abrupt changes in local strain [63]. These waves propagate through the material. Upon reaching the surface, mechanical displacement occurs. The principle of operation of

a piezoelectric AE sensor is that when this happens, the displacement is transferred to a piezoelectric lead zirconate titanate crystal that converts the displacements caused by elastic waves into an electric signal. This process is demonstrated in Figure 10.

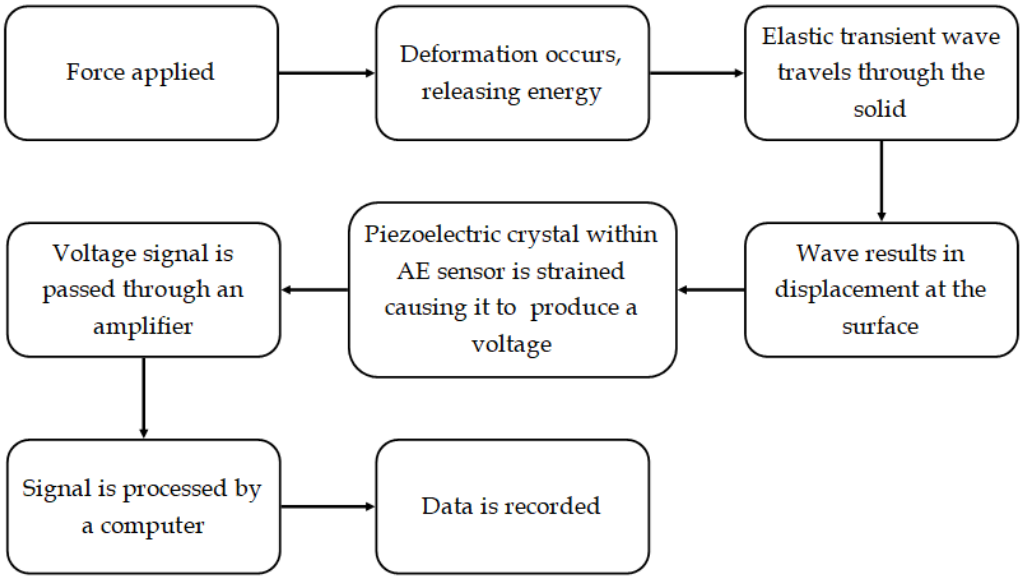

Figure 10: Process flow for measuring an AE event

The diagram in Figure 11 shows the basic structure of a typical AE sensor. Once set up, an AE sensor can be left to collect data without intervention by an operator. After it has been mounted and coupled onto the surface of a material it can remotely and continuously record data from damage evolution as it occurs. Because measurements are taken as rolling stock travel over the rail, inspection performed with a mounted AE sensor does not impact rail traffic (in contrast to other inspection methods).

Rails can remain in service for years or even decades depending on traffic levels. Obviously this is a long time for continuous monitoring, with a large amount of data potentially being recorded, especially in an environment

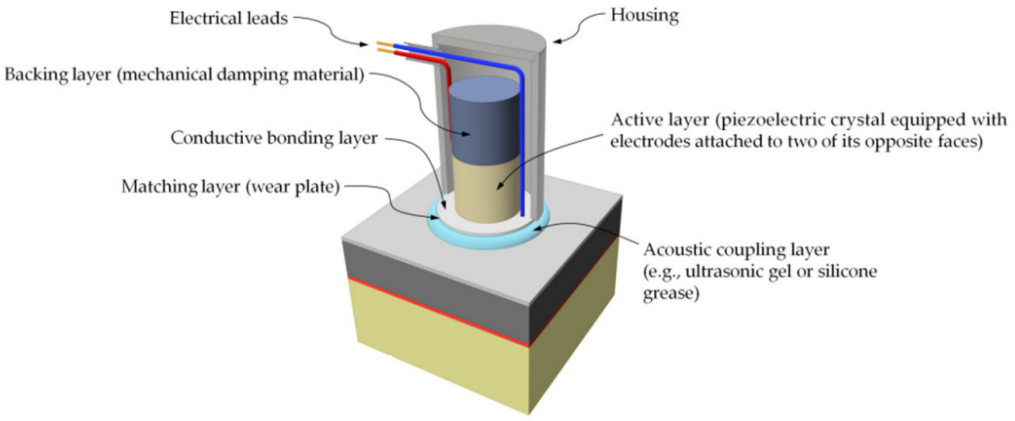

Figure 11: Internal diagram of an AE sensor [10].

where a lot of noise is generated. However, there are potential solutions to this. In rails, defect growth is caused by high loads as train wheels pass over. With the addition of train detection equipment, it is possible to limit AE measurement to these moments to reduce the amount of data collected. Each AE event can also be simplified from its waveform to a summary of its parameters such as those demonstrated in Figure 12. Although some data is lost in the process, parametric data is much easier to interpret, particularly with regards to the change in AE over time which can provide valuable data on health degradation.

Events which generate AE include cracking [64, 65], plastic deformation (primarily due to dislocation movements) [66–69], and corrosion [70]. The characteristics of the energy that is acoustically emitted by a deformation event depend upon:

- The type of damage occurring (in crack nucleation and propagation, the produced AE is made of pulses/distinct events whereas plastic defor-

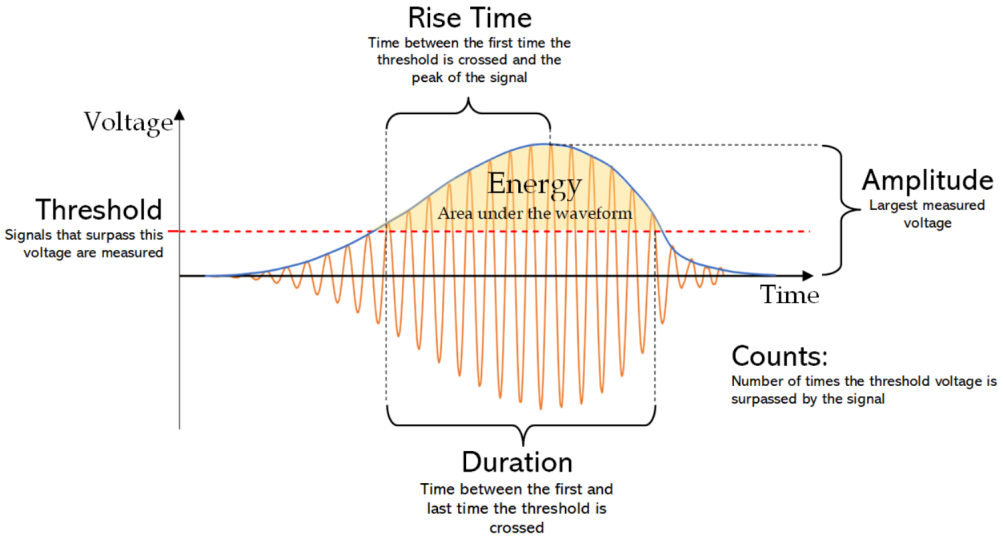

Figure 12: Some parameters that can be used to simplify a measured acoustic emission event

mation can generate a continuous stream of overlapping, low-amplitude AE events).

- The loading conditions. For example, shear loading can produce slanted events [71].

- The severity of the event. For example, a higher crack propagation rate will result in a signal of higher intensity due to more energy being released.

The characteristics of the measured voltage waveform (inspection output) depend upon:

- The characteristics of the deformation event (see above).

- The material, geometry, and relative position of the AE sensor which all influence the attenuation. This is where the intensity of an AE wave

is reduced as it travels through a medium. Therefore, the longer the distance from the AE source to the sensor, the less the surface will be displaced when the wave reaches it (and subsequently the lower the measured amplitude will be when the piezoelectric crystal is strained).

- The equipment used (piezoelectric of the sensor crystal, amplification, resolution, sampling rate, and signal processing).

It was concluded by Eitzen and Wadley that in steel, plasticity cannot typically be measured using AE. This is because the energy released by a single dislocation movement is not large enough to surpass surrounding noise. It will therefore only be measured during mass dislocation movement, such as when a weld deforms, where the magnitude of the combined AE is sufficiently large [63].

AE events expected to be produced and measured within a metal undergoing fatigue crack growth are a result of crack propagation, crack closure, and friction. In rail application, these sources are likely to dominate the produced AE as other rail deformation is primarily plasticity-related.

The energy measured by AE is not equal to the energy released as the damage occurs for several reasons:

- It is calculated by integrating the voltage produced as the piezoelectric crystal is deformed inside the AE sensor. It is therefore dependent on the piezoelectric properties of the crystal and is given in V^2s.

- The sensor measures the waves propagated to a particular point rather than the total energy produced. The wave also must travel through the

material to reach the sensor meaning that the measured wave will be affected by attenuation and will be a function of the material properties, component geometry, and distance from the AE source to the sensor.

- As shown in Figure 12, the energy is calculated as the area under the wave outline but above the voltage threshold. The value therefore excludes energy produced by the wave below this point.

Interpretation of AE in terms of relating the recorded levels of AE energy released into damage evolution requires an amount of calibration for a specific application scenario.

AE can be analysed using its statistical analysis of selected AE parameters or through waveform analysis. Waveform analysis on in-service rails has successfully been shown to be capable of identifying areas of low health, although it is more difficult to interpret than its simplification into parametric data from a quantification perspective [72–74].

It has also been shown that waveform analysis of an AE sensor attached to a rail can be used to detect poor wheel and axle bearing health of passing railway rolling stock [72, 75]. Abnormal AE signals produced by damaged rolling stock can be distinguished from AE resulting from rail damage using fused features of Shannon entropy and RMS (Root Mean Square).[75]

2.2.2 Defect Location using Acoustic Emission

A benefit of AE is that very small crack growth can be detected without having to directly seek out the defect. AE is passive in nature, meaning that defects can be detected as they occur due to the signals they release

and their location can be discerned using signal data from multiple sensors. Localisation is based upon Equation 1 where s is the distance between the AE source and a sensor, V is the velocity at which the wave propagates through the material (which is constant for a homogeneous medium), and T_T is the time taken for the AE to be detected by the sensor after it has been released at the source.

$$s = V * T_T \tag{1}$$

On its own, one sensor cannot be used to find the time taken for an AE signal to reach it it because there is no reference point. Multiple sensors placed a known distance apart must instead be used in order to compare the time at which a particular signal was measured. Potential source locations can then be calculated based upon this time difference and the location of each sensor.

Full location of the source of an AE wave within a three-dimensional space requires 4 sensors [76]. In the case of a bar (where the length of a monitored part far exceeds its width or height) it is sufficient to use two sensors as this can be used to find the longitudinal location. As rails are of bar type geometry, defects can be detected and sufficiently located by sensors placed at intervals along the rail.

If the sensors are placed too far apart, attenuation may result in AE events being missed by one or both sensors either side of where the event is occurring. The intervals between sensors should therefore be optimised to avoid this whilst keeping the number of sensors needed along the length of

track relatively low. It has previously been found that for rail steel attenuation is acceptable where sensors are positioned in the magnitude of tens of meters away from the AE source, depending on the sensor used [77].

2.2.3 Quantitative Analysis of Crack Size Using AE Signals

Although AE is established as a method of detecting and locating actively occurring damage, using it to quantify the extent of the damage is not as straightforward as in other inspection methods such as visual inspection or magnetic flux leakage (MFL). This is because the data are collected and output as a function of time rather than, for example, mapping damage as a function of position on the rail. Nevertheless, research over the last few decades has been performed to determine the quantification potential of AE. This has primarily been focused upon calculating the length of a growing fatigue crack through analysis of the change in AE parameters over time in signals relating to both crack propagation and crack closure.

Crack Propagation AE Signal Quantification

Crack propagation signals have been found in laboratory testing to relate to crack growth occurring at the time. Under fatigue loading, the change in counts and energy measured per cycle have been shown to relate to ΔK through the empirical relationships shown in Equations 2 and 3 in metals such as steel [78–80], Incoloy [81], and aluminium [82, 83] alloys. ΔK is the stress intensity factor range, N is the number of cycles, C_P and E_P are respectively the counts and energy measured during crack propagation and

β_0, β_1, γ_0, and γ_1 are experimentally fitted constants. The form of these equations is very similar to Paris's Law which is shown in Equation 4 where a is the crack length, and C and m are material constants.

$$\frac{dC_P}{dN} = \beta_0 * \Delta K^{\beta_1} \tag{2}$$

$$\frac{dE_P}{dN} = \gamma_0 * \Delta K^{\gamma_1} \tag{3}$$

$$\frac{da}{dN} = C * \Delta K^m \tag{4}$$

This relationship has also been observed in pearlitic rail steel in laboratory testing to varying success. While the relationship between $Log\Delta K$ with $Log\frac{dC_P}{dN}$ and $Log\frac{dE_P}{dN}$ is often shown to generally be positive, the extent to which it is linear varies considerably [15, 65, 73, 81, 84, 85]. Different grades of pearlitic steel also appear to follow Equations 2 and 3 to varying extents. For example in an experiment by Culwick, these relationships were observed to be stronger in R220 steel than R260 steel [15]. In some studies, as the crack reached critical length the trend appeared to plateau. The relationship was also weaker in all studies than the Paris's relationship.

In Hadfield steel, $Log\Delta K$ does not appear to have a simple linear relationship with $Log\frac{dC_P}{dN}$ and $Log\frac{dE_P}{dN}$. Previous research has instead indicated that the AE rates appear to either bear no apparent relationship to ΔK or show an negative correlation at lower ΔK values followed by a positive correlation at higher ΔK values [15, 73, 86].

Combining Equations 2 and 3 with Paris's relationship through ΔK provides equations for theoretical relationships between the AE parameter rates and the crack growth rate as shown in Equations 5 and 6. B_0, B_1, Γ_0 and Γ_1 are constants which combine the constants in Equation 2 and 3 with the constants in Equation 4.

$$Log\left(\frac{da}{dN}\right) = Log(B_0) + B_1 * Log\left(\frac{dC_P}{dN}\right) \tag{5}$$

$$Log\left(\frac{da}{dN}\right) = Log(\Gamma_0) + \Gamma_1 * Log\left(\frac{dE_P}{dN}\right) \tag{6}$$

Several fatigue AE studies have also shown this relationship to reasonable success in Incoloy [81], aluminium [82], and steels [83] including pearlitic grades of rail steel [11]. These studies typically saw a fairly strong linear relationship between $Log\Delta K$ and both $Log\frac{dC_P}{dN}$ and $Log\frac{dE_P}{dN}$ making their conformity to the relationship given in Equations 5 and 6 unsurprising. Typically, where studies have not found a strong relationship with $Log\Delta K$ and $Log\frac{dC_P}{dN}$ or $Log\frac{dE_P}{dN}$, the relationship between $Log\frac{dC_P}{dN}$ or $Log\frac{dE_P}{dN}$ with $Log\frac{da}{dN}$ is not shown.

Equations 5 and 6 give a relationship between the AE parameters and the absolute increase in crack length. Once the constants are known (these may vary depending on factors such as equipment and section of the rail being measured), an estimate for absolute crack length can be calculated if the initial size of the crack at the beginning of AE monitoring is known. Equations 7 and 8 show a direct calculation of the increase in crack length using AE parameters.

$$\Delta a = \int_{N_0}^{N_f} B_0 * \left(\frac{dC_P}{dN}\right)^{B_1} \tag{7}$$

$$\Delta a = \int_{N_0}^{N_f} \Gamma_0 * \left(\frac{dE_P}{dN}\right)^{\Gamma_1} \tag{8}$$

An assumption made in Equations 5 to 8 is that Paris's law is followed, which is only true in the intermediate stage of growth. They are therefore inaccurate while a crack is very small or approaching failure.

Crack Closure AE Signal Quantification

AE signals are not only produced during crack propagation, but also crack closure. Crack closure occurs in scenarios where the loading ratio is below ~0.45. At low loads the sides of the crack meet and rub together, deforming and releasing energy [87]. In application, rails are subjected to high maximum and low minimum loads meaning that crack closure can be expected to occur.

The energy released during crack closure depends upon conditions such as material properties and load ratio as well as the crack surface area. If the testing conditions are consistent and known, the energy can be used to calculate the surface area and therefore the crack length. Unlike quantification using crack propagation related AE, the absolute length of a crack can be calculated from a short period of monitoring. Based upon this principle, Li et al. showed that the count and energy rates measured during crack closure in U71Mn rail steel followed the relationships shown in Equation 9 [11]. δ_0,

δ_1 and δ_2 are constants, and C_c is the counts measured during crack closure.

$$a = \delta_2 \left(\frac{dC_c}{dN}\right)^2 + \delta_1 \left(\frac{dC_c}{dN}\right) + \delta_0 \tag{9}$$

Assuming that δ_0, δ_1 and δ_2 are known, the crack length can therefore be estimated from a short period of AE monitoring.

Comparison of Crack Propagation and Crack Closure Quantification

Figure 13 shows a comparison between the use of propagation versus closure related AE to determine the size of a crack. It can be seen that where crack-closure related AE is used to find crack length, the estimate fluctuated around the true value whilst for crack-propagation related AE the error accumulated. The primary benefit of using crack closure AE is that the calculation can be performed at any stage of life without prior knowledge of crack length.

However, the empirical crack propagation relationships are better established. More research is required to determine the consistency and applicability of the mentioned crack closure relationships.

The constants used to calculate crack size in both methods are dependant on the material as well as the testing conditions. In order to successfully apply the equations for a given application, it is therefore necessary to calibrate these values to the materials and to the scenario.

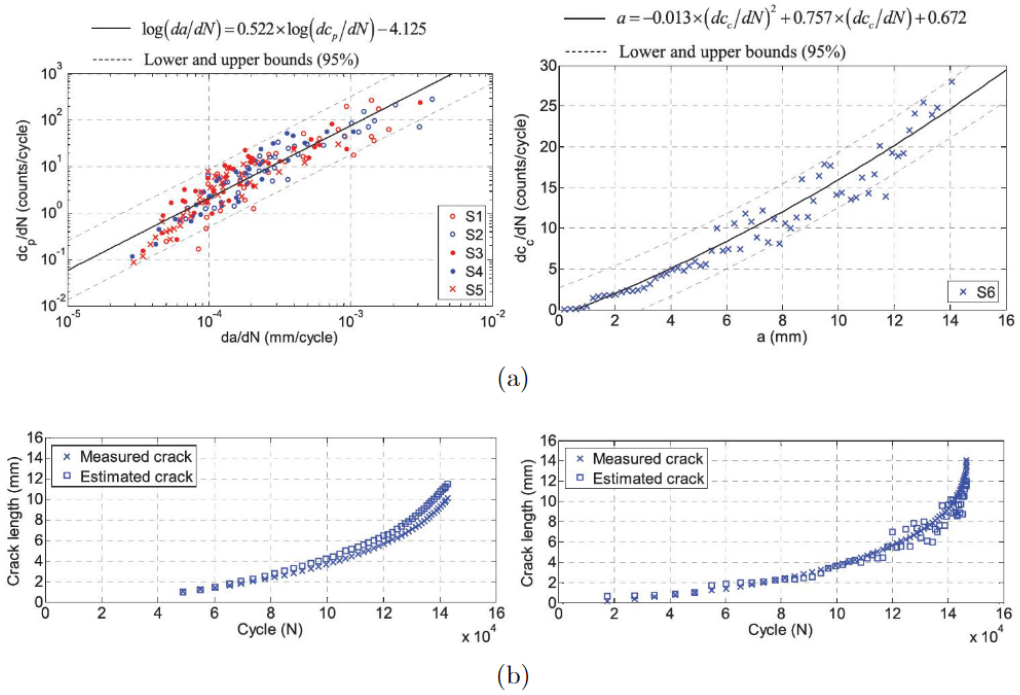

Figure 13: Acoustic Emission and its translation into crack length for a pearlitic rail steel (U71Mn). a) Relationships between $\frac{dC}{dN}$ and the crack length for crack propagation and closure related AE (left and right respectively). b) Crack length estimations from the measured acoustic emission for crack propagation and closure related AE (left and right respectively) [11].

2.2.4 Qualitative Analysis of Cracks Using AE Signals

Observation of cumulative AE parameters can also provide valuable information about crack growth. It has been observed that counts and energy follow a relatively similar trend to the crack length when plotted against cycles [12, 72, 73, 84]. The graphs typically follow a step-wise motion and previous work directly associated some of these steps with inclusions along the crack face which are thought to result in fast crack growth [12]. An example of this is given in Figure 14.

This shows that not only does AE have the capability to detect, locate

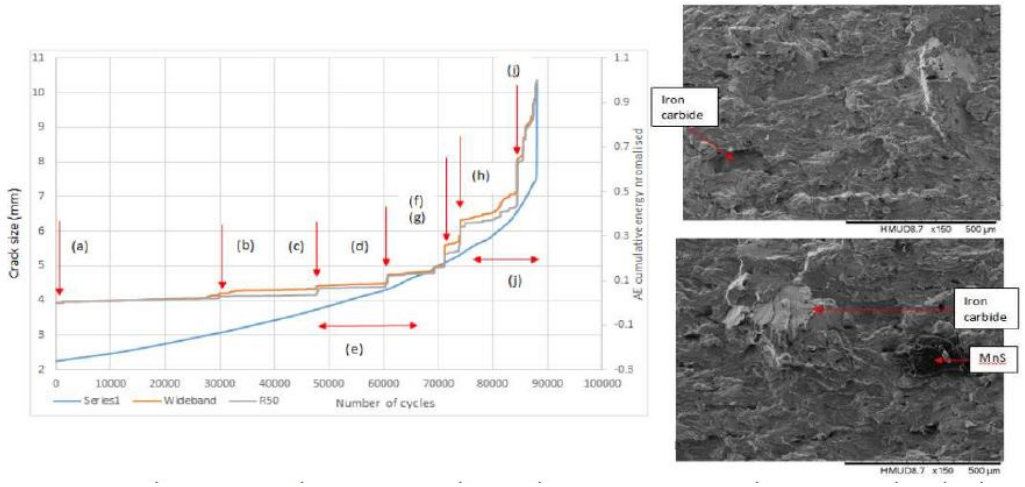

Figure 14: Cumulative AE energy and crack length plotted against cycles. The top micrograph corresponds to the step seen at (f) and the bottom micrograph corresponds to the region (e) [12].

and quantify cracking, but also to provide information on the microstructure that the crack tip has reached.

2.2.5 Other Analysis of Acoustic Emission

AE has also previously been related to cyclic hardening and internal friction. In copper single crystal samples, a strong linear relationship was found between the average power of measured AE and the cyclic hardening rate as shown in Figure 15 [13]. An equation defining this relationship is given in [13].

In marble specimens under low cycle fatigue, AE energy parameters have been related to cumulative damage under tensile load to failure by Equation 10. This equation relates the damage to the proportion of energy that has already been measured to the cumulative energy value at which failure oc-

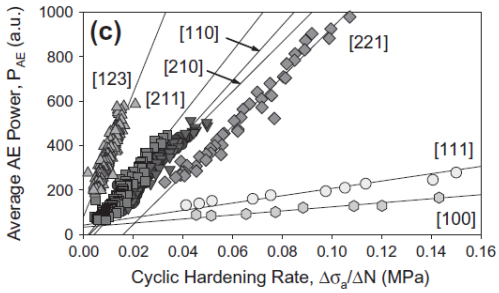

Figure 15: Relationship between AE power and the cyclic hardening rate of copper single crystal samples [13].

curred. σ_{eq} is theoretical stress, E is Young's modulus, ϵ is strain, n is the current AE event number, i is a count of the event number, e_i is the event energy, and E_f is cumulative AE energy at failure [88].

$$\sigma_{eq} = E\epsilon(1 - \frac{\sum_{i=1}^{n} e_i}{E_f}) \tag{10}$$

Using Equation 10, the AE provided stress estimations of reasonable accuracy, although it did not reproduce the observed softening [88]. Although this relationship has only been observed in marble, it shows how cumulative parameters can be used to aid quantification of structural damage.

2.2.6 Limitations of Acoustic Emission as a Monitoring Tool

Although numerous relationships between AE and damage have been observed during laboratory testing, it is important to consider that during application in rail and crossing monitoring the measurement conditions would be less favourable. For example, there is significantly more noise as a rail is loaded by a train axle compared to a sample in three point bending loaded by a pin. If noise is prevalent and is not sufficiently filtered, the damage may

be overestimated. In contrast, if filters are set too high then valuable damage propagation related data may be lost and damage may be underestimated. This means that in application conditions, effective signal processing is even more imperative.

In addition, the way in which damage propagates through the material is also likely to be different than in the tests that provided these relationships. For example, in previous laboratory tests loading was applied cyclically meaning that Paris's law was followed for crack growth. During use, however, rails are exposed to stochastic loads where crack growth behaviour is more complex. Therefore Equations 5 to 8 could not be used in their current format. As well as this, cracks that are seen in rails often branch and are of more complex geometry than the straight cracks that are tested during bending fatigue tests. Nevertheless, it is important to identify and define these simpler relationships before moving into more complex quantification.

All mentioned relationships are purely empirical and have been reached through observing the relationships in experimental data. It is argued by Nazarchuk, Skalskyi and Serhiyenko that many studies relating AE to damage do not classify the signal into its constitutive parts, rendering their scientific value low or insignificant [89]. However, if empirical relationships are found to consistently provide accurate information for the state of a given material, regardless of fully understanding the mechanisms by which it works, they provide valuable tools for assessing consistent behaviour and can be used as inputs for models. In other words, if an input (AE) is known to consistently produce a particular output (e.g. crack growth, plastic deformation) then it can be very useful even without fully understanding why it occurs.

2.3 Modelling of Rail Steel

2.3.1 Background to Modelling Rails

Whilst periodic monitoring of rail tracks can provide information of its present health in the instant that inspection is performed, the health of the rail between inspections is unknown. Modelling is a method that can be used to lower the uncertainties within these gaps. The development of models to a maturity where there is a high confidence in the results could vastly reduce the frequency at which inspections are required and thus reduce the associated costs and disruption to services. The addition of continuous monitoring such as AE could additionally facilitate the development of digital twins which represent a best estimate of current rail health.

In order to build this confidence, it is important to understand the conditions that rails are exposed to and how they deform in response. These conditions and their resulting influence on the material must both be translated into a model which should reproduce the behaviour to an acceptable accuracy.

For the highest confidence, accuracy must be prioritised. However, this comes at the price of computational effort. For a long lifetime component such as rails, efficiency is a requirement in order to keep the time and associated costs at a manageable level.

There are currently no functional real-time digital twins for rail track health monitoring. To achieve this a model must use an input of measured data from the physical component that is being modelled to determine conditions for the simulation. This input could be information on the loading

that is being applied to the rail, where the same loading can then be applied to the model. It could also be an inspection output such as AE data, where the degradation information could be translated into the model (e.g. crack propagation or material softening). The output would then be an estimated current state of the rail.

Aside from being developed to reproduce expected behaviour, models can also be used to identify and explain particular behaviours that might be observed in different scenarios. Benefits of modelling compared to experimental testing include the ability to: recreate severe conditions that must be avoided in application, analyse the internal stresses throughout the test, and to observe how the behaviour is altered as individual variables are changed. However, the accuracy and usefulness of analyses such as these depends upon the setup of the model, including any assumptions and simplifications that are made.

2.3.2 Modelling Rolling Contact Fatigue (RCF) crack growth in rail steels

Several models have previously been created to predict crack growth from the surface of a rail due to RCF. Set-ups have included simplified rail and wheel [51, 52, 90, 91] and twin disk [92] geometries, and have modelled the growth of a cracks in their intermediate stage of growth. Some models used purely elastic behaviour [51, 52, 90–92] while others included plastic deformation [93]. By nature, the formation of head checks during RCF is a plastic process, and the directional growth is known to be heavily influenced by residual stresses [94]. It is therefore arguable how accurate models that assume

isotropic elastic behaviour can be. For example, in a model by Brouzoulis et al. simulated cracks only grew upwards, which is known to not always be the case [52]. It was noted that the inclusion of plasticity and anisotropy would provide a truer representation of crack behaviour at the expense of significant extra computational effort [52]. RCF cracks that grow downwards are more serious than those that grow upwards and therefore it is important to correctly determine the direction of growth in a given scenario [50].

Work has also been done to investigate pressure-driven crack propagation due to the presence of fluid. 2D and 3D FEA models of simplified rail and wheel geometries were used to simulate crack growth in dry and wet conditions. These studies showed that the occurrence of fluid entrapment can cause mixed-mode shear dominated growth. They also demonstrated that the correct conditions of braking force, residual stresses and initial angle can cause a crack to grow in the mode I direction [51, 90, 91]. The presence of fluid was shown by Bogdanski to cause a K_I 8 times greater than that observed without fluid as a wheel passes over the rail [90]. When analysing the stress intensity factor components for cracks in both dry and wet conditions, analysis parameters such as co-efficient of friction and inclusion of tractive force were observed to produce significantly different values for K_I and K_{II} [50, 90].

There are limitations to the present research, including the common assumption of Paris's Law (where the loads applied to rails are typically stochastic), elastic isotropic behaviour (rails undergo work hardening), and the consideration of single cracks in isolation (the reality for RCF cracks in rails is typically a network of many small cracks). These works are valuable

for understanding the growth mechanisms behind theoretical cracks but for the application of a digital twin it would be important to also understand the overall degradation of the microstructure.

2.3.3 Modelling the cyclic response of rail steel

For the majority of rail life, no cracks are present/evident. However, the high loads that are applied to the rails by passing wheels cause local plasticity and deformation. Research into modelling the cyclic response of rail steel has primarily been based on small plate/disk samples. A model that is commonly used for rail steel is the Ohno-Wang (OW) model [95] for kinematic hardening along with the Abdel-Karem-Ohno (AKO) model [96] which combines OW with the Armstrong-Frederick (AF) model [97] to simulate steady state ratcheting under cyclic load [49, 98–100]. It has been found that for rail steel, the AKO model performs better than its constitutive parts, with the OW model unable to predict uniaxial ratcheting without other ratcheting present and the AF model providing less accuracy for plasticity [99].

In 2020, Meyer performed an analysis on four models (Meyer - based upon AF and Burlet-Cailletaud (BC) [97], Shi [101], Qin [102], and Crystal Plasticity [103]) to compare their performance when modelling a rail steel sample under cyclic loading. The model by Shi provided the lowest fitting error to experimental results. However, it also overestimated softening in the loading direction and did not accurately reproduce the rotation and translation of the yield surface (which was better captured by the Qin model). It was concluded that no single model was accurate in all aspects [100]. In later work, Meyer et al. developed a new stress-driven model, MM2021, which

was shown to fit the plastic anisotropy of the rail steel samples even better without an increase in computational effort [104].

Modelling has also previously included thermal affects due to friction at the rail-wheel interface. In 2021, Esmaeili et al. used the Armstrong-Frederick model whilst also incorporating thermal expansion strain and transformation expansion strain [105].

Surface plasticity has also been directly modelled as wheel-rail interaction. The added complexity of more complex geometry and contact modelling means that the computational effort required for such simulations is significantly higher. El-Sayed et al. used a small section of simplified rail and wheel geometries to investigate crack initiation. The Chaboche and Lemaitre (CL) model [106] was used, which performs less accurately for rail steel than models such as AKO and MM2021 but is also less complex with fewer material parameters used. CL behaviour was also confined to a small region while the rest of the model assumed elasticity to increase efficiency. The model provided a crack initiation estimate of 1.3 million cycles and was shown to reproduce contact conditions reasonably accurately whilst minimising computation effort [106–109]. The same model was also able to predict the angle of crack initiation on the railhead which was validated by physical rail analysis [107]. In another approach, Meyer et al. used periodic boundary conditions and the MM2021 model to achieve a wheel-rail interaction model with efficiency around 25 times that of other models of similar accuracy [104, 110]. This model was shown to be capable of including discontinuities and capturing plastic accumulation.

Difficulties in modelling and validating material models for rail steel in-

clude the anisotropy and behaviour gradient from the surface of the head downwards [6, 20, 34, 35]. Not only does the hardness and strength change with the interlamellar spacing of pearlite, but so too does the hardening behaviour (see Figure 5) [6]. To the author's knowledge, no rail model exists that takes this varying hardening behaviour into account.

2.3.4 Modelling and AE

There are not yet any FEA models that translate AE into damage or crack growth. However, the reverse of producing AE events from modelled crack growth has been applied. These models are used to gather information on the magnitude of AE waveforms, the types of waves that are produced, and how these waves propagate through a material [111–116]. The potential benefits of such models include sensor placement and spacing optimisation, better information on how structural features cause scattering, and to aid development of advanced signal filtering (i.e. to remove noise) [117, 118].

A difficulty encountered when investigating these waveforms, however, is that the models cannot be fully validated. The AE wave produced at the source may be very different to the one that is read from the AE sensor due to influences from both the material that the wave must travel through as well as how it is translated to, and processed by, the sensing equipment as previously discussed. In the context of rail application, it is unlikely that the use of waveforms on this scale is applicable due to the noise experienced as well as the large time-frame over which deformation occurs.

Parametric AE data has also been compared to FEA models. Yeh et al. compared the AE counts released by Inconel samples containing differ-

ent crack lengths for the same applied force. It was found that due to the dependence of energy emission on crack-tip plastic volume, the calculated J-Integral values showed an almost linear relationship with the AE counts released when the force was applied [119]. This technique, however, would be difficult to reverse engineer into a digital twin.

2.4 Literature Summary

Rails stay in service for a matter of years or even decades. The exact lifetime of rails and crossings is based on the conditions such as loading, environmental aspects, and the health of the rolling stock which uses it. Rail tracks are safety-critical and rail or crossing failure can result in high economic cost due to both the damage caused and the resulting disruption to travel.

Rail steel and Hadfield steel (used at crossings) are inhomogenous due to both manufacture and work hardening during application. The loading conditions are stochastic and the force distribution can change over time, depending on factors such as the rail and wheel geometry (which can change with wear), and how safely the rail is attached to the sleepers and the ballast. Hadfield steel is used at crossings due to its better resistance to wear and impact loads. It has a strong propensity to work harden.

Inspection of rails is currently performed on a periodic basis using a variety of methods that can accurately quantify defects. However, they require access to the rails which can result in disruption to rail services, particularly as demand for rail is increasing. Acoustic emission is a passive, continuous monitoring technique that can be remotely assessed. It has been shown

to have excellent detection and location capabilities as well as reasonable quantification abilities for crack growth, hardening and damage.

Failure in rails is complex and its prediction is difficult. Currently used quantification inspection techniques provide a snapshot of health each time they are used. Without implementing some type of predictive aspect for rail life, the condition of rails between inspections is unknown and the uncertainty of current health is a function of time since the last inspection. There are several approaches that could be used to combat this:

1. Inspecting tracks at a conservative frequency results in reasonably high confidence as the degradation between inspections is minimised. However, it is expensive and more disruptive to travel.

2. Application of a continuous monitoring system such as AE inspection would reduce the uncertainty between inspections by providing data on degradation as it occurs. However, with the technology in its current maturity, the confidence in quantification is much lower than that which is provided by other inspection methods.

3. Modelling anticipated degradation from the state the rail was in at the time of the previous inspection could be used to estimate the current and future state of the rail based upon anticipated loading scenarios. However, the loads applied to rails are hard to predict and stochastic meaning that any unexpected loading events (e.g. an impact load caused by a severe wheel flat) would not be accounted for; a conservative approach would have to be taken.

4. Creating a digital twin which takes continuous data and uses it to update a model. This combines points 2 and 3 where a model of the rail (in the state it was most recently assessed to be in) uses monitoring data to continuously or periodically update, reflecting an estimate of current health.

3 METHODOLOGY

3.1 Acoustic Emission Analysis of Three-Point Bending Fatigue Crack Growth

Three-point bending (TPB) fatigue tests were carried out on samples of cast manganese steel and R260 rail steel to measure AE during crack propagation. Each sample was notched using spark wire erosion. Precracks were initiated using an Amsler vibrophore cyclically loading between 0.65 and 6.5 kN at the resonant frequency of approximately 100 Hz. Figure 16 shows a typical notch with a pre-crack, demonstrating the initial state of each sample.

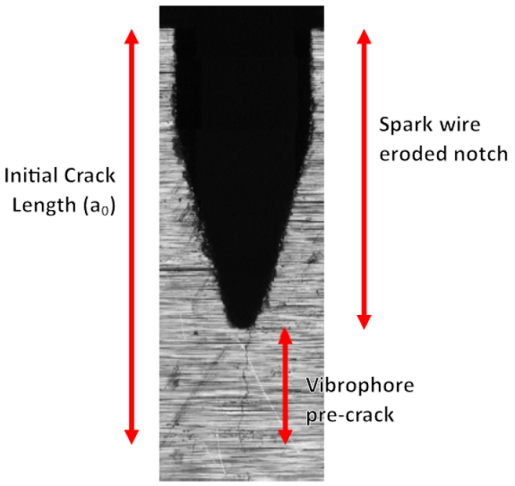

Figure 16: Annotated notch and pre-crack. Taken from [14] which was adapted from [15].

The experimental setup is shown in Figure 17. The bottom pins were displaced to apply a sinusoidal load between P_{min} and P_{max} at a constant frequency allowing the fatigue crack to grow until final failure. The AE sensors were attached using Araldite (an epoxy adhesive).

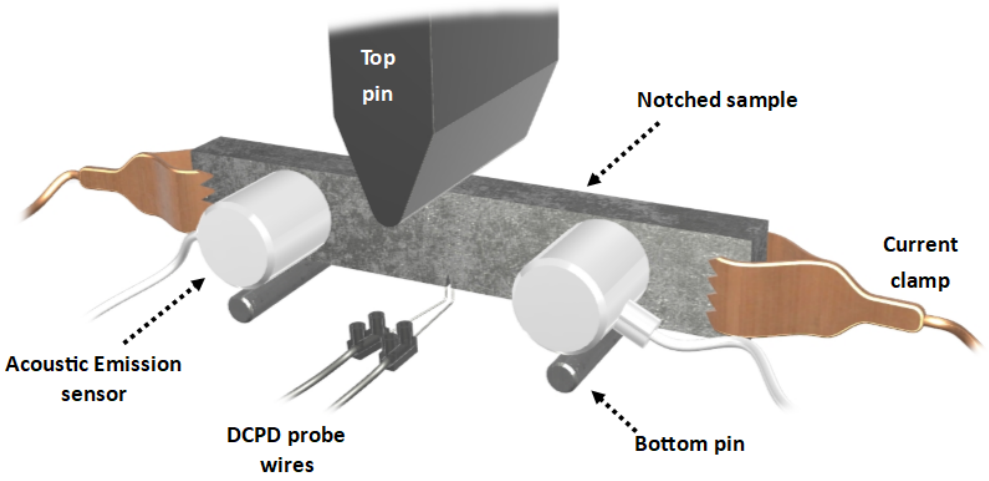

Figure 17: Annotated diagram of the three point bend experimental setup with simplified geometry, not to scale.

DCPD was used to continuously output the crack length. A current was passed through the sample using clamps, and spot-welded probes around the notch were linked to a strip chart recorder. These charts were later scanned and data was read using WebPlotDigitizer, a digital data extraction tool [120]. These values were then translated into crack length using Johnson's formula as shown in Equation 11. Symbol definitions and values are given in Table 4.

$$a = \frac{2W}{\pi} cos^{-1} \left(\frac{cosh\left(\frac{\pi y}{2W}\right)}{cosh\left(\frac{U(a)}{U(a_0)} cosh^{-1}\left[\frac{cosh\left(\frac{\pi y}{2W}\right)}{Cos\left(\frac{\pi a_0}{2W}\right)}\right]\right)} \right) \tag{11}$$

The stress intensity factor range was calculated for comparison with the AE data. Equation 12 (which is relevant to the TPB conditions) was used to calculate K_{Min} and K_{Max} using P_{Min} and P_{Max} respectively for each data

point of crack length [121]. ΔK was then found using Equation 13. The definitions and values of each symbol are given in Table 4.

Table 4: Symbol definitions and values for crack growth and stress intensity factor calculations

Attribute	Description	Value Type	Units
a	Crack length	Calculated	m
a_0	Initial crack length	Measured	m
W	Sample width	0.02	m
B	Sample thickness	0.01	m
U	Voltage	Measured	V
U_0	Initial voltage	Measured	V
y	Half DCPD probe distance	Measured	m
P_{Min}	Minimum load	Input	N
P_{Max}	Maximum load	Input	N
K_{Min}	Minimum stress intensity factor (where $P = P_{Min}$)	Calculated	$MPam^{\frac{1}{2}}$
K_{Max}	Maximum stress intensity factor (where $P = P_{Max}$)	Calculated	$MPam^{\frac{1}{2}}$
ΔK	Stress intensity factor range	Calculated	$MPam^{\frac{1}{2}}$

$$K = \frac{4P}{B}\sqrt{\frac{\pi}{W}}\left[1.6\left(\frac{a}{W}\right)^{\frac{1}{2}} - 2.6\left(\frac{a}{W}\right)^{\frac{1}{2}} + 12.3\left(\frac{a}{W}\right)^{\frac{5}{2}} - 21.2\left(\frac{a}{W}\right)^{\frac{7}{2}} + 21.8\left(\frac{a}{W}\right)^{\frac{9}{2}}\right] \tag{12}$$

$$\Delta K = K_{Max} - K_{Min} \tag{13}$$

In order to investigate the stage of each loading cycle at which hits were measured, the time data was translated into cycles (using the frequency) and

calibrated by associating the time at which the hits were measured to the force that was measured at the time (for the Hadfield samples this was also validated using identifiable peaks in the waveform data). The loading cycle is demonstrated in Figure 18 (using the example of the Hadfield steel loads). Therefore in the analysis 0 to π was defined as loading while π to 2π was defined as unloading.

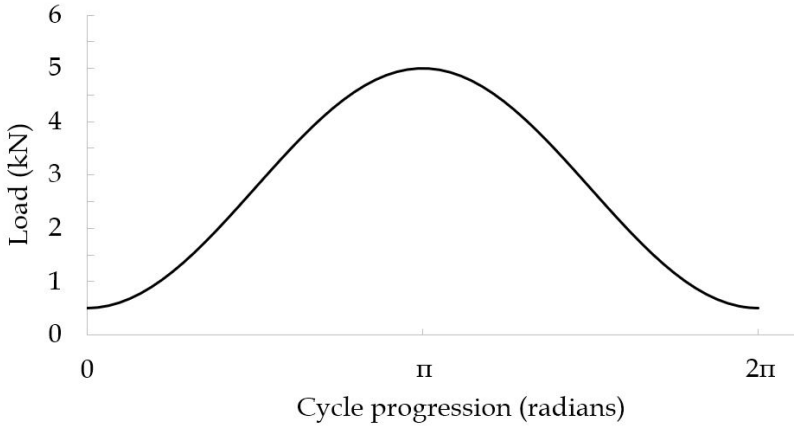

Figure 18: The three point bending test loading cycle for the Hadfield steel samples in radians.

In the results, energy is defined as the output voltage integrated over time and therefore has units of V^2s. For simplicity (and in line with convention) arbitrary units (a.u.) are used instead. Any AE event with an energy of 0 a.u. was excluded from all analyses due to such events being considered insignificant.

3.1.1 Cast Manganese Steel Samples

Ten samples were cut from a cast manganese steel (also known as Hadfield steel) plate to the geometry shown in Figure 19. As the material had not been

loaded prior to precracking, the samples were not initially work hardened.

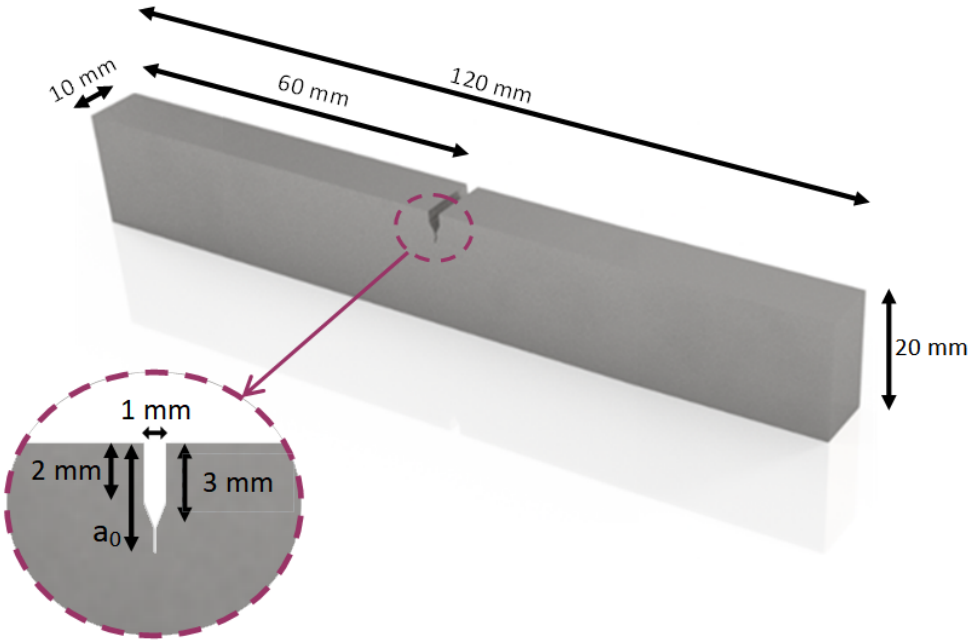

Figure 19: The sample geometry used for the Hadfield steel samples. a_0 is the total length of the pre-crack. The angle of the notch was 30^o. Prior to pre-cracking the notch tips were rounded with a radius of 0.12 mm.

P_{Min} and P_{Max} were 0.5 kN and 5 kN respectively and the input frequency was 5 Hz. However, during calibration to find the cycle stage it was found that a more precise value for the frequency was 5.00337 Hz. This value was used to calculate cycles and cycle stage with better precision, which was necessary due to the high number of cycles to final failure (N_F).

AE was measured by two R50a resonant piezoelectric sensors. From one the full waveform data was recorded while from the other events were simplified into parametric data. The sensor used for each task remained the same throughout the test. The AE sampling rate used for both sensors was 1 MHz. The waveform sensor took 5 second recordings at 5 second intervals.

3.1.2 R260 Rail Steel Samples

Data from an AE monitored three point bending test of R260 steel had already been obtained and the data analysed in [14] with regards to the cumulative counts and energy as well as the count rates and energy rates. In this project some additional analysis has been performed into the cycle stage of detected AE as well as the amplitudes measured throughout the test.

Ten samples were cut from a rail that had been removed from use and had therefore been work-hardened. Details on their geometry along with the filtering used are given in [14]. P_{Min} and P_{Max} were 0.65 kN and 6.5 kN respectively and the input frequency was 1 Hz. However, during calibration to find the cycle stage it was found that a more precise value for the frequency was 1.000674 Hz. This value was used to calculate cycles and cycle stage with better precision (which was necessary due to the high number of cycles to reach N_F). Due to the high number of cycles to failure and the low frequency used, most samples were tested over several days with pauses in between due to experimental restrictions related to safety measures in place.

3.2 Model of Crack Propagation through Rail Steel containing an Inclusion

The experimental observation of links between steps in cumulative energy and the point at which a crack grows through a soft sulphide inclusion in rail steel [12] was investigated using Finite Element Analysis (FEA). Three point bending of a cracked R260 sample that contained an inclusion was simulated in order to compare the calculated energy release to the AE which

was measured experimentally. Where relevant and possible, the model was based upon the conditions in [12]. This work is also reported in [19].

As previously mentioned, the energy recorded from AE measurement has the units V^2s and is calculated as an integration of the measured voltage. The energy output by ABAQUS is given in J and is a theoretical value of the actual energy released. Because of this, the two values cannot be directly related with regards to magnitude. However, the change in the values of both over time can be compared and related. In addition, it is possible that in future work these values could be calibrated to allow a translation of magnitude between the two.

Geometry and Setup

The sample geometry and setup is shown in Figure 20. To simplify the model, it was simulated in two dimensions. Values were therefore calculated relative to the section (i.e. per 1 μm thickness). The inclusion was placed centrally within the sample and at a depth of 5 mm from the bottom surface of the rail. Its dimensions and geometry were simplified from micrographs of MnS inclusions in the literature [122, 123]. A separate version of the model that did not have an inclusion but used the same mesh was also performed for comparison.

The model was created in ABAQUS and was performed as a static structural analysis. All pins were defined as rigid. The bottom two pins were fixed in position. Horizontal shifting of the sample was prevented by constraining the center of the sample in the horizontal direction.

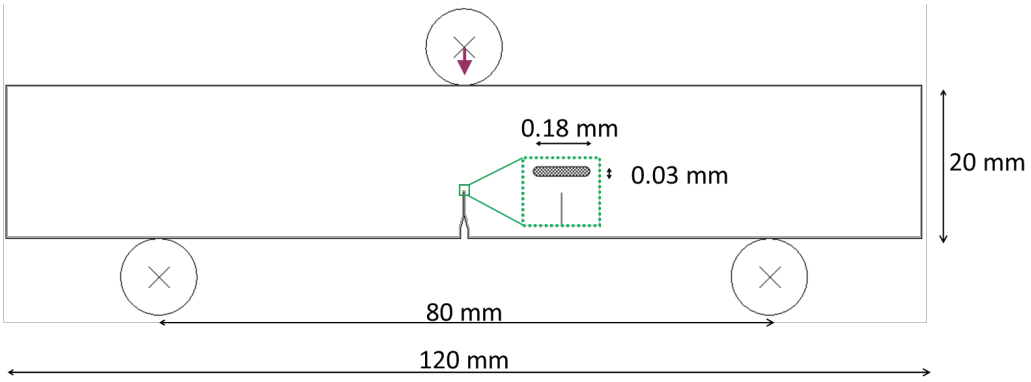

Figure 20: The setup of the three-point bending FEA model detailed in this report. The green square shows a detail view of the sample geometry.

A ramp displacement of 0.15 mm was applied to the top pin, forcing it down onto the sample. This was done over a time period of 1 second, which was arbitrarily chosen. The contact between each pin and the sample was defined as hard and frictionless.

The in-built extended finite element method (XFEM) was used for crack growth. It was chosen in order to avoid the requirement to re-mesh throughout the simulation and so that the crack was free to grow in any direction.

The maximum time increment was set as 0.01 s to ensure that the analysis could converge.

Mesh

The mesh was comprised of around 27500 CPS4 linear quadrilateral elements which is shown in Figure 21. This included a finer mesh around the anticipated crack growth path, particularly near to and inside the inclusion as shown in Figure 22.

This mesh was considered suitable to provide a proof of concept for linking

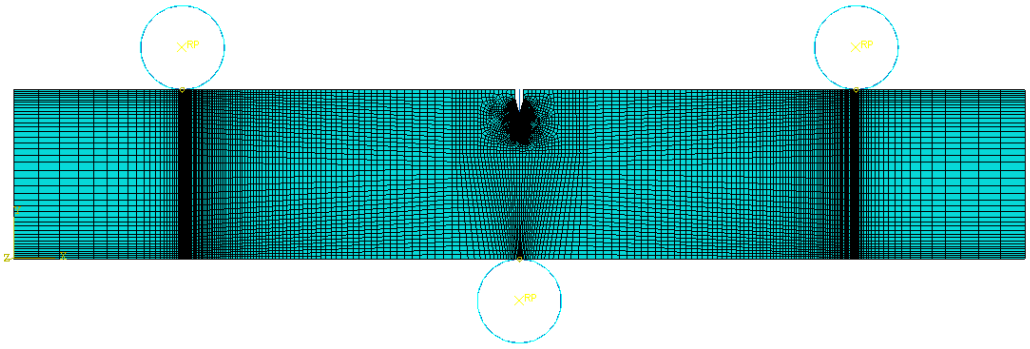

Figure 21: The FEA mesh created in ABAQUS.

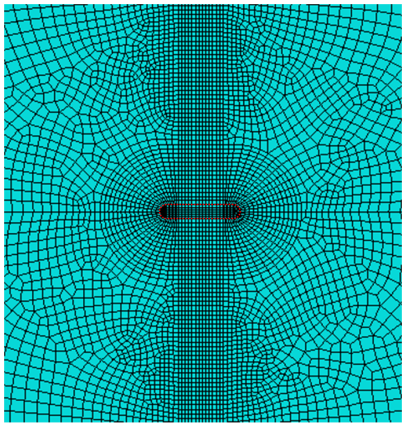

Figure 22: The fine FEA mesh around the inclusion (outlined).

experimental AE data to FEA-calculated energy. In future work this mesh could be further refined and created in three dimensions to ensure optimum accuracy of the calculated outputs. However, this falls beyond the scope of this thesis.

Material Definitions

The matrix material was defined as R260 rail steel, as this was the material in which a step in AE was linked to the location of an inclusion in [12]. ABAQUS's inbuilt Johnson Cook Hardening was used to model its plasticity

[124]. This behaviour is shown in Equation 14 where σ_{eq} is the equivalent stress, D_1 is the initial yield strength, D_2 is the strain-hardening coefficient, $\dot{\epsilon}$ is the strain rate, $\dot{\epsilon_0}$ is the reference strain rate, ϵ_{pl} is the plastic strain, n is the strain hardening exponent, D_3 is the strain rate sensitivity, and T^* is a temperature function ($\frac{\dot{\epsilon}}{\dot{\epsilon_0}}$ and T^* were taken as 1 and 0 respectively) [124].

$$\sigma_{eq} = \left[D_1 + D_2\epsilon_{pl}^n\right]\left[1 + D_3 Ln\left(\frac{\dot{\epsilon}}{\dot{\epsilon_0}}\right)\right][1 - T^*] \tag{14}$$

The properties of the soft sulphide inclusion were based upon MnS which is a common inclusion seen in R260 rail steel. Where specific properties of MnS could not be found in the literature, they were based upon ZnS instead (another soft sulphide). The properties used for R260 steel and the inclusion are summarised in Table 5. Both were defined as homogeneous. The values for fracture energy (G_{IC}) were calculated using Equation 15 after finding values in the literature for fracture toughness (K_{IC}) and Young's modulus (E) of each material [125].

$$G_{IC} = \frac{{K_{IC}}^2}{E} \tag{15}$$

Table 5: Material properties used in the inclusion model. Table taken from [19] which used values found in references [20–25].

Property	**Model Units**	**R260 Steel**	**Sulphide Inclusion**
Young's modulus	MPa	202 x 10^3	27.3 x 10^3
Poisson's ratio	-	0.3	0.38
Tensile strength	MPa	951	50
Fracture toughness	$MPam^{\frac{1}{2}}$	38.56	1
Fracture energy	$mJmm^{-2}$	7.53	36.6 x 10^{-3}
Initial yield strength	MPa	528	-
Strain-hardening coefficient	MPa	1662.8	-
Strain-hardening exponent	-	0.54	-

Output Requests

To enable XFEM crack growth, the field outputs PHILSM and PSILSM were requested. In order to record the energy change within the model, the history outputs relating to energy released during crack growth (ALLDMD) and the energy dissipated during plastic deformation (ALLPD) were also requested. A small region was defined which encompassed all crack growth and plastic deformation related to crack growth and the energy data was obtained from this area. This was done so as to avoid any additional plastic deformation energy resulting from the contact between the sample and the pins from being included in the results. This can be justified by the ability of AE inspection as a location tool. AE data recorded can similarly be used to distinguish between sources of AE.

4 RESULTS AND DISCUSSION

4.1 Acoustic Emission Fatigue Test in Three-Point Bending

4.1.1 Cast Manganese Steel

General Experimental Observations

All samples were successfully tested to final failure. A summary of initial and final crack length in each sample along with the number of cycles before failure are shown in Table 6.

Table 6: The pre-crack length (a_0), length at failure (a_f) and cycles to failure (N_f) for ten Hadfield steel samples.

Sample	a_0 **(mm)**	a_f **(mm)**	N_f
1	4.916	14.363	63558
2	3.336	11.519	115459
3	3.442	10.988	68612
4	2.906	9.876	86749
5	2.872	10.188	91165
6	2.998	10.720	72032
7	3.062	9.780	61367
8	2.960	10.230	62651
9	3.221	11.461	82407
10	2.623	8.867	66169

The initial crack length (a_0) in each sample has been plotted against cycles to failure (N_f) and crack length at failure (a_f) in Figure 23. It can be observed that a_0 appeared to have a positive correlation with a_f whilst seeming to be independent of N_f. This suggests that the crack growth rate and critical crack length was influenced by material deformation during pre-cracking

where the maximum load and frequency were both larger than during the fatigue test. Due to the inherent ability of Hadfield steel to work-harden, it is possible that the more severe conditions of pre-cracking hardened the material and increased its toughness, therefore increasing the critical crack length.

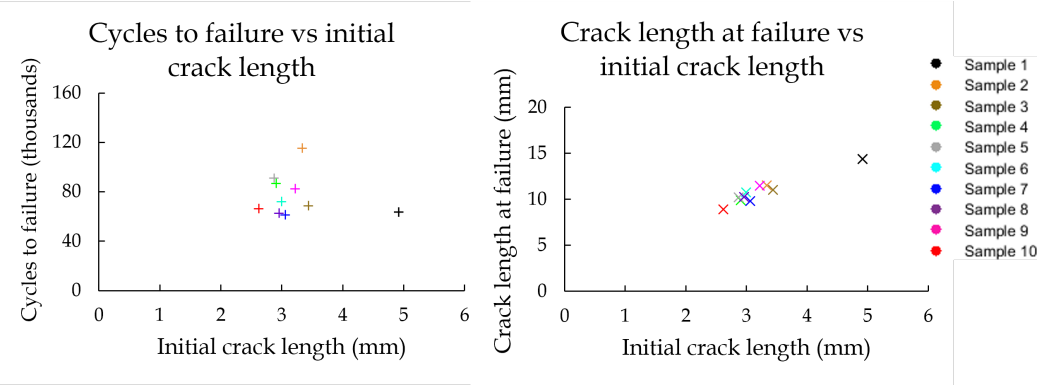

Figure 23: Relationships between the initial crack length (a_0) in each sample with cycles to failure (N_f) (left) and final crack length (a_f) (right).

In contrast to the other samples, Sample 1 fractured into two parts as shown in Figure 24. It can be seen in Table 6 that sample 1 had the longest pre-crack (a_0) as well as the longest crack at failure (a_f), longer than the next longest a_0 and a_f by 43% and 25% respectively. The maximum stress intensity factor (K_{Max}) at a_f was 76.91 $MPam^{\frac{1}{2}}$.

For most samples complete AE data was recorded over the test. The exception was sample 4 where data was lost for a period of the test due to a large amount of data being produced without enough memory to record it. This was because a lot of noise was measured. As a result, data between 42124 and 72914 cycles is not included in this analysis and a higher amplitude filter of 52 dB was used to remove additional noise.

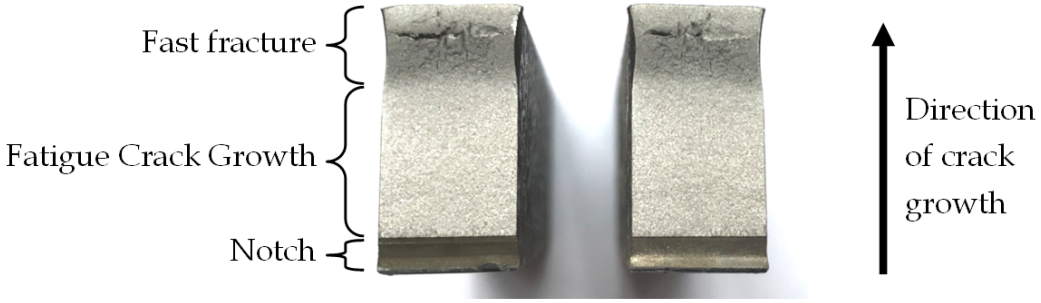

Figure 24: The surface of sample 1 which was the only sample to fracture into two parts. Fatigue crack growth can be clearly distinguished from the fast fracture zone which shows characteristics of ductility.

Cyclic Analysis

The stage of the loading cycle that each hit was measured was translated into the cycle stage (in radians) as demonstrated in Figure 18. This cycle stage value along with the energy measured were used to plot scatter points on polar graphs for each sample as shown in Figure 25. The cycle stage determined the angular value (axis on outer edge) of each point and the hit energy (e_i) determined its radial value (yellow axis). The colour of each scatter point demonstrates the cycle number at which it was measured as a percentage of N_f.

The individual events in Figure 25 were also grouped into 200 bins based upon their cycle stage in order to produce histogram data (shown by the bars in the polar graph). The frequency (F) of hits falling within each band is quantified by the black radial axis.

Comparison between the individual hit data and the histogram data allows easy visual identification of moments in the loading cycle that typically showed many low intensity AE events or few high intensity events.

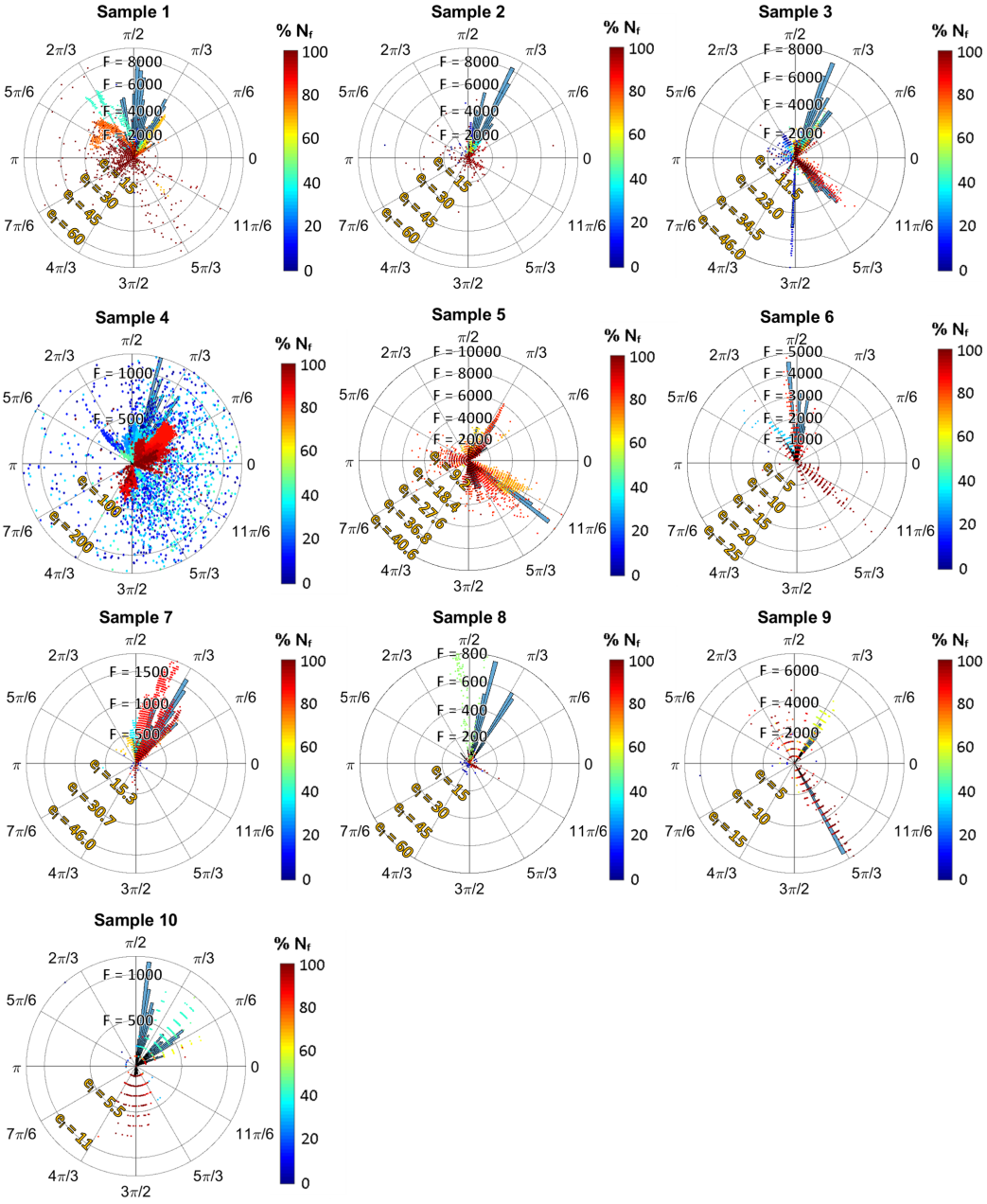

Figure 25: Polar scatter plots (e_i is hit energy) and histogram bars (F is frequency) of the cycle stage at which events were measured as Hadfield steel samples underwent fatigue loading.

It can be observed from the histogram data in Figure 25 that in most samples events were most frequently measured between $\frac{\pi}{3}$ and $\frac{\pi}{2}$ which corresponded to 33% and 55% of the maximum applied force (P_{Max}) in the loading stage. Due to the similar times at which this large amount of hits was measured it is likely that they occurred due to a similar source or mechanism. As they were detected during loading it is likely that these frequently measured events were related to crack propagation and/or friction of crack faces during crack opening.

The scatter points on the graphs allow for the cycle stage at which high energy AE events were measured to be easily seen. It can be observed that this is less consistent across the samples than the histogram data. Clusters of high energy hits did not always coincide with the time in the cycle at which the most events were measured. For example, looking at the polar graph for sample 1 in Figure 25 it can be observed that between $\frac{\pi}{3}$ and $\frac{\pi}{2}$ radians, many events were measured but the energy of each individual event was relatively low. Above $\frac{\pi}{2}$ radians, however, the recorded events were higher in energy but measured less frequently. It can be determined from the colour of the scatter points that as the test progressed, events were measured later in the cycle. This suggests that for the majority of the test, small deformation events were routinely occurring at a cycle stage of between $\frac{\pi}{3}$ and $\frac{\pi}{2}$ radians. Once the crack became more severe the nature of the measured AE changed due to either a change in the crack growth mechanism or a change in the type of AE being measured. The higher energy being released as AE can be explained by larger deformation events occurring as the crack grew (along with ΔK).

It can be observed that samples 3 and 5 frequently produced AE events between a cycle stage of $\frac{5\pi}{3}$ and $\frac{11\pi}{6}$ radians which corresponded to 33% and 16% of P_{Max} during unloading. As these frequently measured events occurred during unloading it is likely that they were caused by crack closure. These events can be observed to have occurred near to failure and were of high energy.

A benefit of plotting polar graphs is that abnormal measurements are easier to identify within a sample. As previously mentioned, the data for sample 4 contained a lot of noise. This can be observed in the polar graph where high energy events appear at each stage of the loading cycle including stages where no hits were measured in other samples. The histogram data, however, shows that a large amount of hits were measured at similar cycle stages to the other samples which related to crack propagation and crack closure, demonstrating the presence of valuable AE data. In order to improve the quality of the data, and therefore quality of quantification, noise removal should be optimised. Future work could involve the use of an algorithm to filter the measured hits based upon the cycle stage. This could be incorporated into a digital twin by measuring the load at which each hit was measured.

To better observe the change in AE over time, the hits were plotted against cycles. The hits versus cycles graphs for all ten Hadfield steel samples are shown in Figure 26. Events that had an energy of 5 a.u. or less are shown in grey; these were considered insignificant and were not included in the AE rate or cumulative analyses below.

Linear trends can be observed at various points in Figure 26 for all sam-

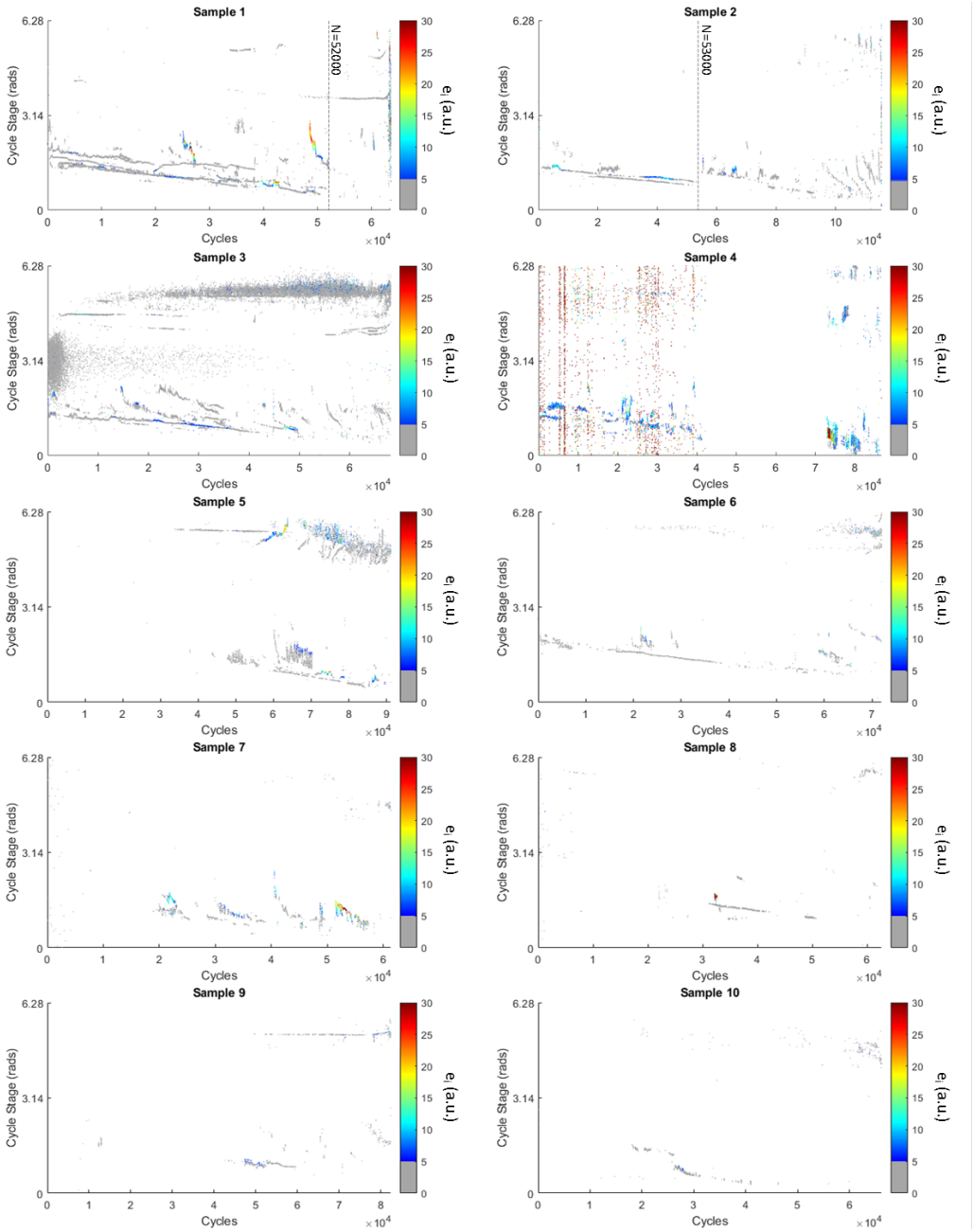

Figure 26: The cycle stage at which hits were measured throughout the fatigue test of each sample. Low energy events are shown in grey. Note that sample 4 is missing data between 42124 and 72914 cycles due to equipment failure.

ples, revealing that hits were often measured at similar times from one cycle to the next. This suggests that AE hits within a trend were produced by a similar, repeating source. Trend lines that appeared during loading (cycle stages below π) can be seen to typically follow a negative correlation with the cycle number meaning that AE hits were measured incrementally earlier each cycle. It can therefore be inferred that the AE source mechanism (crack propagation or friction during crack opening) occurred in an earlier stage of loading as the test progressed and the crack grew.

In a few samples there are also noticeable changes in when AE was primarily measured during the loading stage. For example, after sample 2 was tested to around 53000 cycles, the AE began to be measured at around 0.5 radians later than the trend it had previously been following. There was also a significant decrease in AE hit density after this point with a move from an average of 3.93 hits/second to 1.35 hits/second. The test was performed without any breaks and no factors are known to have changed during the test excluding the crack growth (and ΔK as a result). This suggests that the nature of the measured AE changed as a result of the crack length which could indicate that the crack growth was altered due to a change in microstructure at the crack tip or a change in crack growth mechanism.

For sample 1, AE was observed to initially occur on loading following a downward trend. After around 52000 cycles, however, this abruptly changed to most events occurring on unloading. It is therefore indicated that up until 52000 cycles, AE was primarily produced as a result of crack propagation, whereas after this point it appears to have primarily been related to crack closure.

Figure 27 shows a detail view of the hits measured during loading between 0 and 60000 cycles for sample 2. There appear to be three distinct trends which have been indicated by coloured circles. The bottom two AE trends (highlighted in green and yellow) have a negative gradient meaning that they occurred at an earlier cycle stage as the test progresses. The top trend (highlighted in pink) was measured only between 20000 and 30000 cycles and had a positive gradient meaning that the AE occurred at a later point in each cycle as the test progressed. Due to the distinct separation of the AE into these trends, it is likely that they were a result of separate events. For example, the bottom (green) trend could be a result of friction or unsticking as the crack opens and the middle trend (yellow) could be a result of crack propagation.

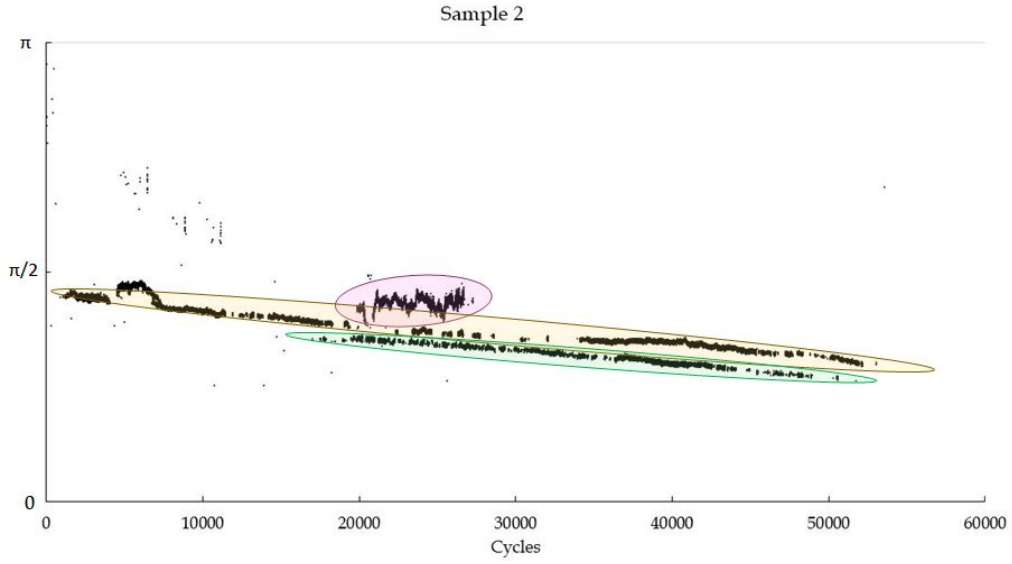

Figure 27: Apparent trends in AE hits in cycles 0 to 52000 of Hadfield sample 2. AE was measured at the same point over many cycles in three clustered lines (highlighted).

Figure 28 shows a sample of four waveforms measured during the fatigue

testing of sample 7. The x axis shows the time relative to the start of the waveform measurement (each waveform sample shown is over 1 s). The first was taken from the start of the test at around 1000 cycles. At this point there were no significant peaks in the signal, suggesting that damage was progressing at a slow rate. This is reflected in Figure 26 which showed very few measured events at the start of the test.

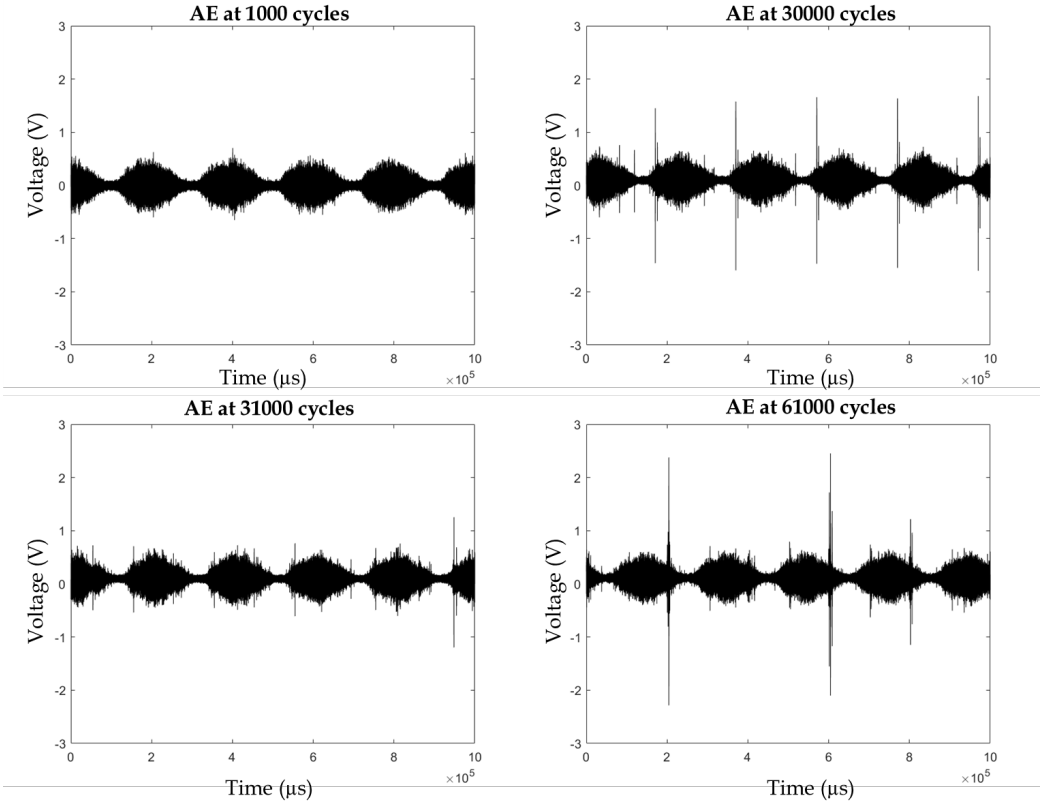

Figure 28: Samples of AE waveforms measured during fatigue crack growth near the start, middle and end of fatigue cracking in sample 7.

Two waveforms are shown from around the midpoint of the test at 30000 and 31000 cycles. Although both signals show peaks, they are significantly larger at 30000 cycles as opposed to 1000 cycles later. These peaks occur on

loading which suggests that they are due to crack propagation. The difference in signal intensity could be explained by a difference in the microstructure through which the crack was propagating, such as propagation through an inclusion (which may increase the speed of crack growth or release a different amount of energy when cracked) or areas that differ in elastic vs plastic crack growth. A detail view of hits measured for sample 7 between 30000 and 40000 cycles is shown in in Figure 29. It can be seen that the signal peaks correspond to the cycle stage at which hits were primarily measured in Figure 28. It can also be seen that the AE appears to follow a pattern of being released over a few hundred cycles followed by a few hundred cycles of no AE activity being measured.

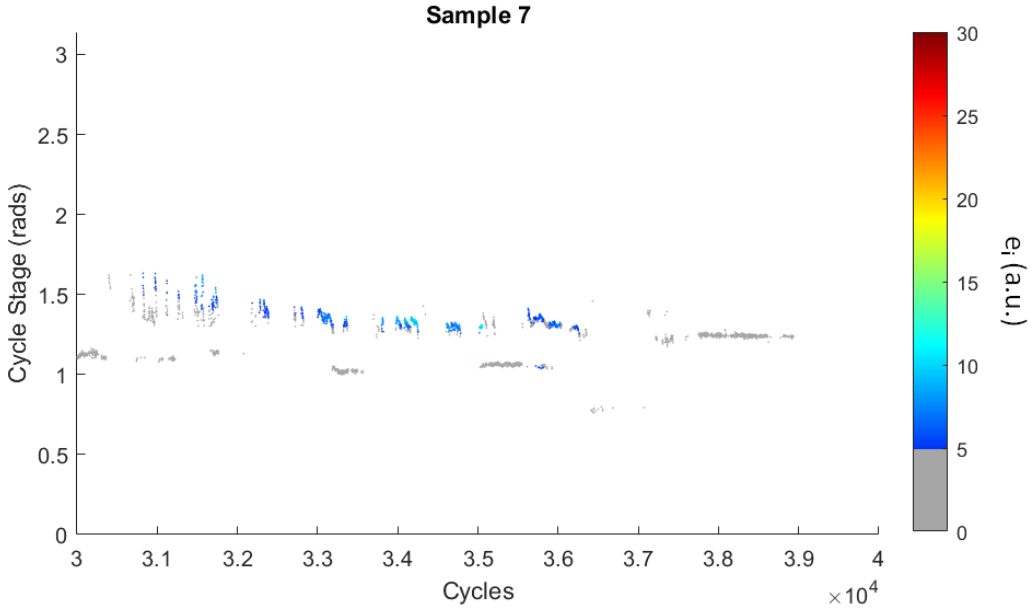

Figure 29: Hits measured between 30000 and 40000 cycles (detail from Figure 28).

The final waveform in Figure 28 was taken at around 61000 cycles, shortly before sample failure. Peaks in the AE signal can be observed on loading and

unloading. The biggest peaks were measured on unloading which is likely to have been a result of crack closure.

$\frac{da}{dN}$, $\frac{dC_P}{dN}$ and $\frac{dE_P}{dN}$ Relationship with ΔK

An analysis into the relationship between the stress intensity factor range (ΔK) with the crack growth rate ($\frac{da}{dN}$), the count rate ($\frac{dC_P}{dN}$) and energy rate ($\frac{dE_P}{dN}$) was performed for all ten Hadfield samples.

In order to reduce the influence of crack closure related AE signals, events which occurred during unloading (at a cycle stage of more than π radians) were excluded. A filter was also applied to remove events that were measured to have less than 5 a.u. energy (the grey plots from Figure 26 which were deemed likely to be related to friction as opposed to crack propagation). Figure 30 shows the observed relationships for the ten samples.

Clear linear behaviour can be observed between $Log(\frac{da}{dN})$ and $Log(\Delta K)$ showing that the sample fatigue crack growth followed Paris's Law (see Equation 4). The plotted linear trend lines have been summarised in Table 7 for reference.

It can be observed that as expected from the literature, there is no clear linear relationship of $Log(\Delta K)$ with $Log(\frac{dC_P}{dN})$ and $Log(\frac{dE_P}{dN})$, although there appears to be some element of a positive relationship, particularly for higher $Log(\Delta K)$ values.

Figure 31 shows a combined graph of count rate and crack growth rate for all samples. The Paris's law behaviour can be observed to be reason-

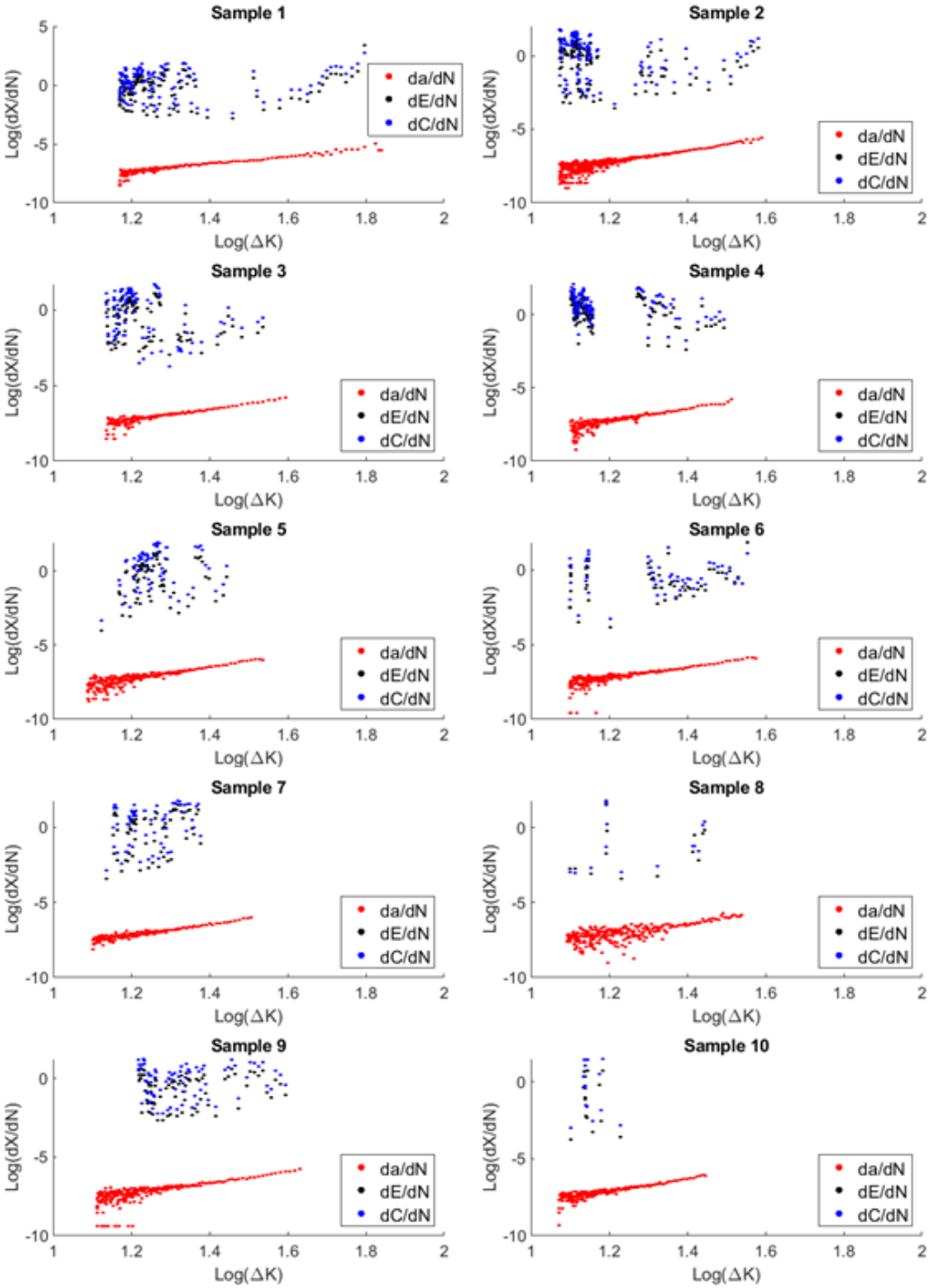

Figure 30: Observed relationships between ΔK, $\frac{da}{dN}$, $\frac{dC_P}{dN}$, and $\frac{dE_P}{dN}$ for ten Hadfield steel samples. Note that AE data is missing for sample 4 between $Log(\Delta K) = 1.18$ to 1.27.

Table 7: Summary of the Paris's Law constants (see Equation 4)

Sample	**m**	**C**
1	2.97	-10.84
2	3.96	-11.99
3	3.53	-11.50
4	4.01	-12.06
5	4.14	-12.26
6	3.55	-11.50
7	3.51	-11.37
8	4.40	-12.60
9	3.16	-11.08
10	4.00	-11.92
Average	3.72	-11.71

ably consistent across all samples, with similar stage II (linear) relationships. However, the combined count rates do not provide a clear resultant relationship. It can therefore be inferred that Equation 2 does not hold true for the Hadfield steel samples in the conditions in which they were tested.

The additional growth of sample 1 can clearly be seen. It can be observed that at a $Log(\Delta K)$ value of around 1.63 (ΔK of 42.7), the crack growth behaviour appears to become slightly more erratic. Crack growth then continued until a ΔK of 76.91 was reached at which point the sample failed in a brittle fashion.

For further comparison, $\frac{dC_P}{dN}$ was plotted against $\frac{da}{dN}$ in Figure 32. If $Log(\frac{dC_P}{dN})$ had shown a linear relationship with $Log(\Delta K)$ then this relationship would similarly be reasonably linear (due to the Paris's law behaviour of growth - see Equation 5). The count rate could then be used to estimate the crack growth and therefore the total crack length (assuming a_0 was known). However, no clear relationship was observed between $\frac{dC_P}{dN}$ and $Log(\Delta K)$; it

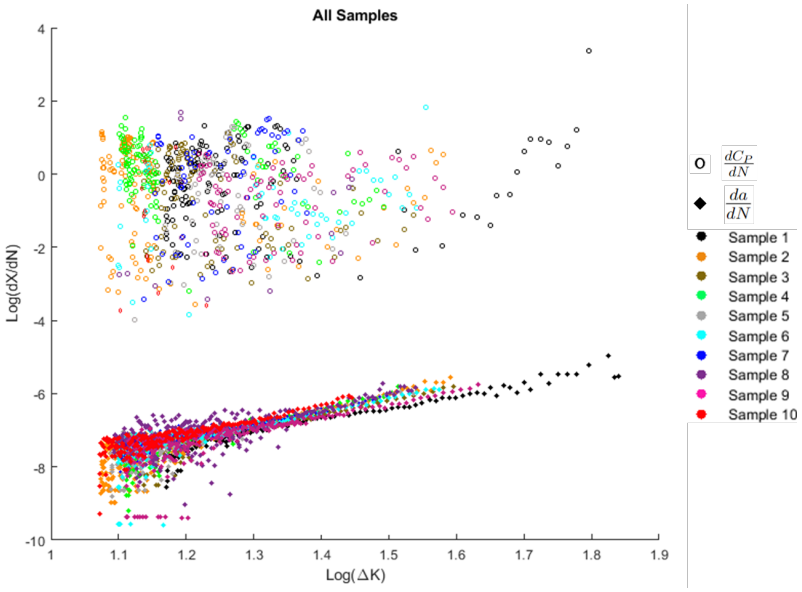

Figure 31: Crack growth rate ($\frac{da}{dN}$) and count rate ($\frac{dC_P}{dN}$) relationship with ΔK for ten Hadfield steel samples.

is therefore unsurprising that when plotted against $\frac{da}{dN}$ there is no apparent relationship. The empirical relationship given in Equation 5 was therefore not observed.

The lack of linear relationship between $Log(\frac{dC_P}{dN})$ and $Log(\frac{da}{dN})$ meant that Equation 7 could not be used to calculate an estimation for the crack length.

Cumulative Counts and Energy

Cumulative counts and energy measured whilst cracking the Hadfield steel samples are plotted alongside crack length in Figure 33. In the majority of samples, a step-wise increase in cumulative counts and energy was observed. An exception to this is sample 4. This is likely to be due to the noise that was encountered for this sample.

The cumulative counts and cumulative energy both closely mirrored each

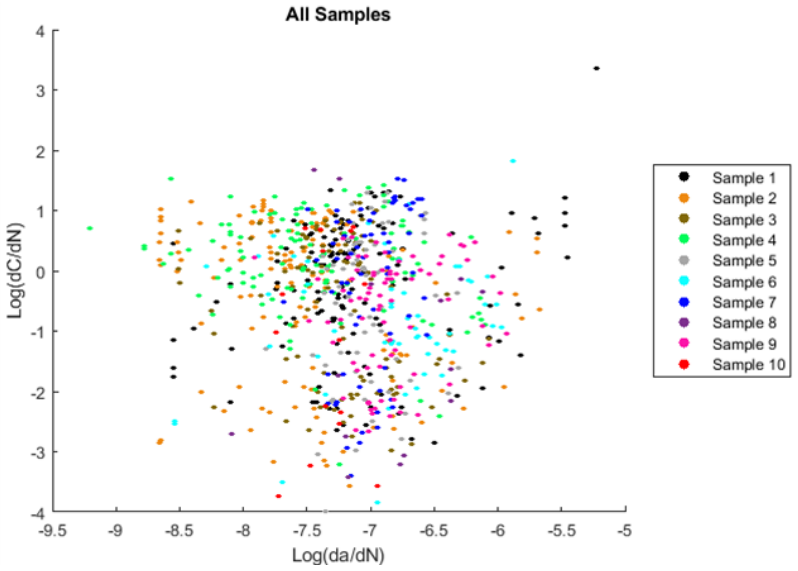

Figure 32: Count rate ($\frac{dC_P}{dN}$) plotted against crack growth rate ($\frac{da}{dN}$) for ten Hadfield samples.

other. The ratio of counts to energy is reasonably large in all samples excluding sample 8 in which the values were similar. There is also only 1 significant step in the plot at 32000 cycles which corresponds to the cluster of hits seen in Figure 26.

It can be noted that in several samples (1,3 and 7) the cumulative counts and energy are a similar shape to the crack length. In sample 9, the cumulative counts after around 50000 cycles appear to follow the crack length plot closely. To an extent, cumulative graphs can provide another way of gauging the severity of fatigue crack growth.

Amplitude

The amplitude of each hit over the test for each Hadfield steel sample is shown in Figure 34. No common theme was observed between all ten samples. In

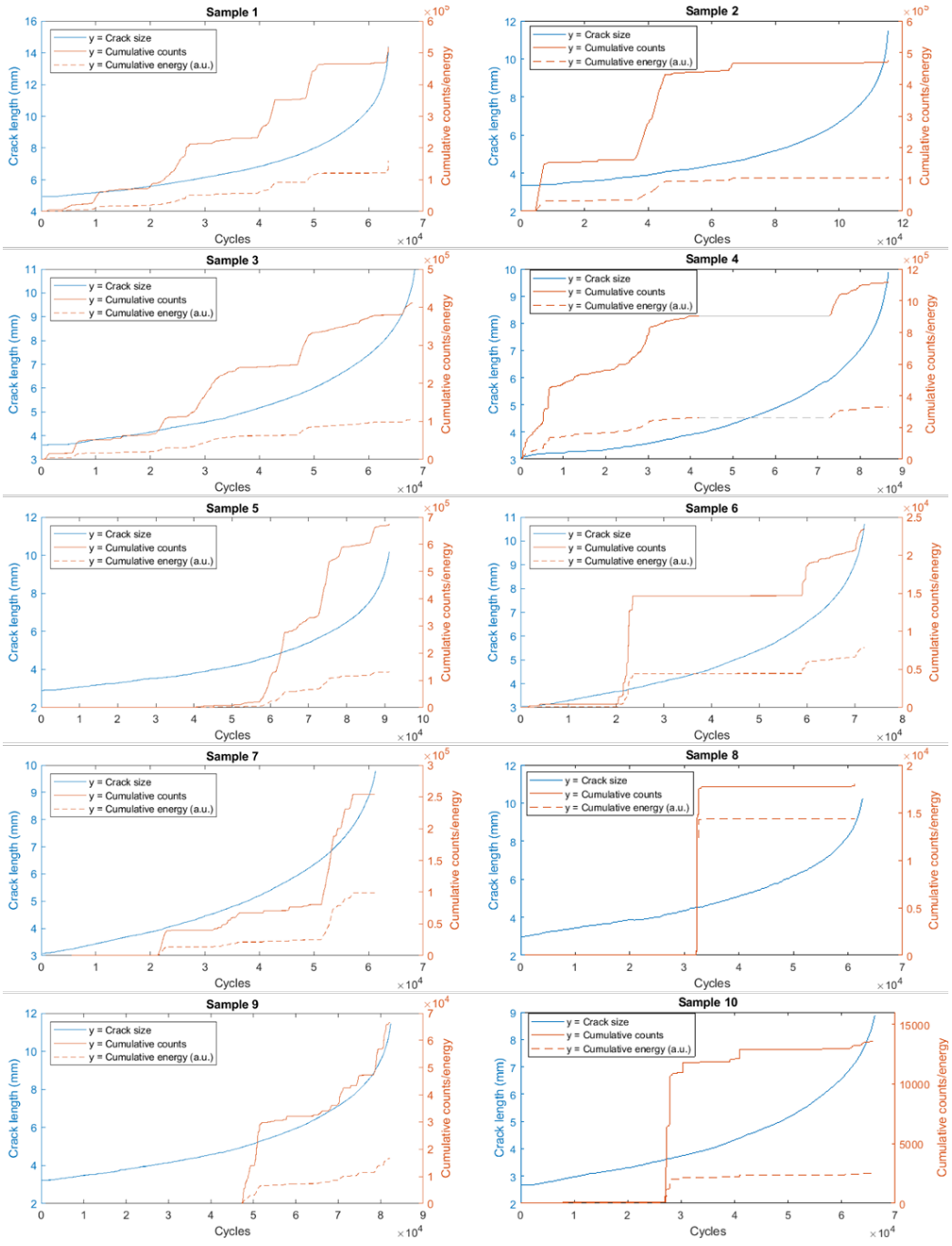

Figure 33: Cumulative AE counts and energy plotted against cycles alongside crack length. The grey plateau in sample 4 identifies missing data.

samples 1 and 2 there were hits of very high amplitude immediately prior to failure. This is similar to what has previously been observed in Hadfield steel in similar experimental conditions [73, 86]. However, this was not observed in any other samples which instead had higher amplitude hits at various points throughout the test. Previous work has referred to these high amplitude hits as "alarms" hinting at imminent failure. However, their absence in most of these results highlights that this should not be relied upon. In multiple samples it can be observed that the measured amplitudes seem to decrease soon before failure (most noticeably in sample 1). This is most likely due to increased plasticity at the crack tip which results in lower amounts of measurable AE [63].

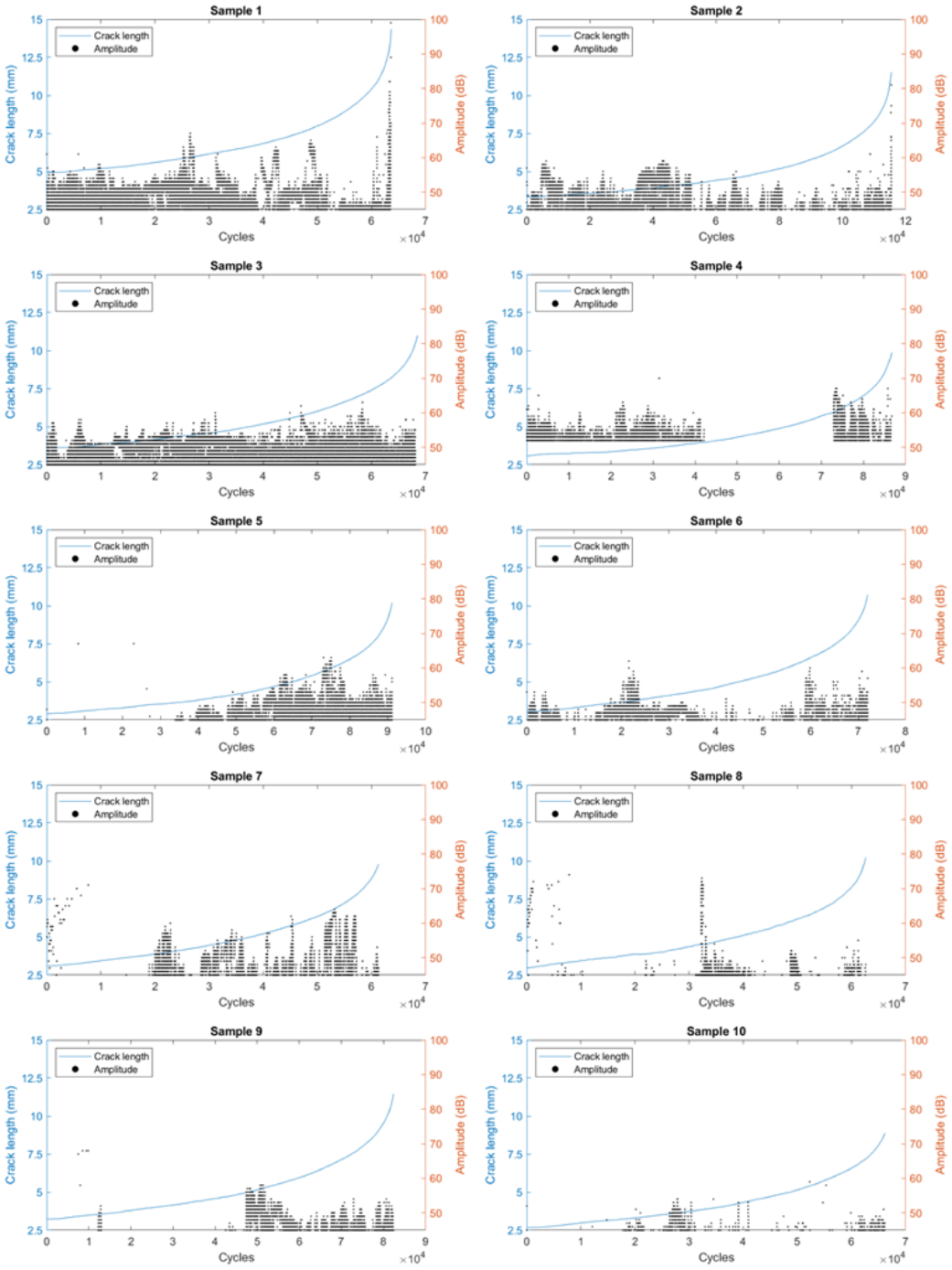

Figure 34: Amplitude of the AE signal for ten Hadfield samples with the crack length also shown. Sample 4 is missing data below 52 dB due to necessary noise removal.

4.1.2 R260 Steel

Cyclic Analysis

The cycle stage at which AE events were measured throughout the testing of the R260 samples was analysed and polar graphs were produced to show both individual events and histogram data. These polar graphs were created in the same way as previously described in the Hadfield steel samples analysis section.

The amplitude measurement threshold for sample 1 was initially set too low at 45 dB which resulted in a lot of noise within the data. The AE before and after applying an additional amplitude filter was used to look at the cycle stages at which noise was measured and to see if plotting the cycle stage can help to validate noise removal. Figure 35 shows cycle stage that hits were measured before and after an additional amplitude filter was applied.

The histogram data shows that at low amplitude filtering, the vast majority of hits were measured between $\frac{\pi}{2}$ and $\frac{3\pi}{2}$ radians. This makes sense, as it was when the machine exerted the highest loads on the sample. Not only were the noise-related hits measured often, but they also were high in energy. If left in, this noise would dominate the data. In contrast, after the data was filtered below 52 dB, it can be seen that there are very few hits within the previously noise filled region. This shows that filtering was successful, and how using the visual aid of the cycle stage can help to identify and validate noise removal in cyclic testing. However, it would not reveal the extent to which true AE signals were lost within the noise during filtering.

Figure 36 shows the polar cycle stage and histogram data for all ten

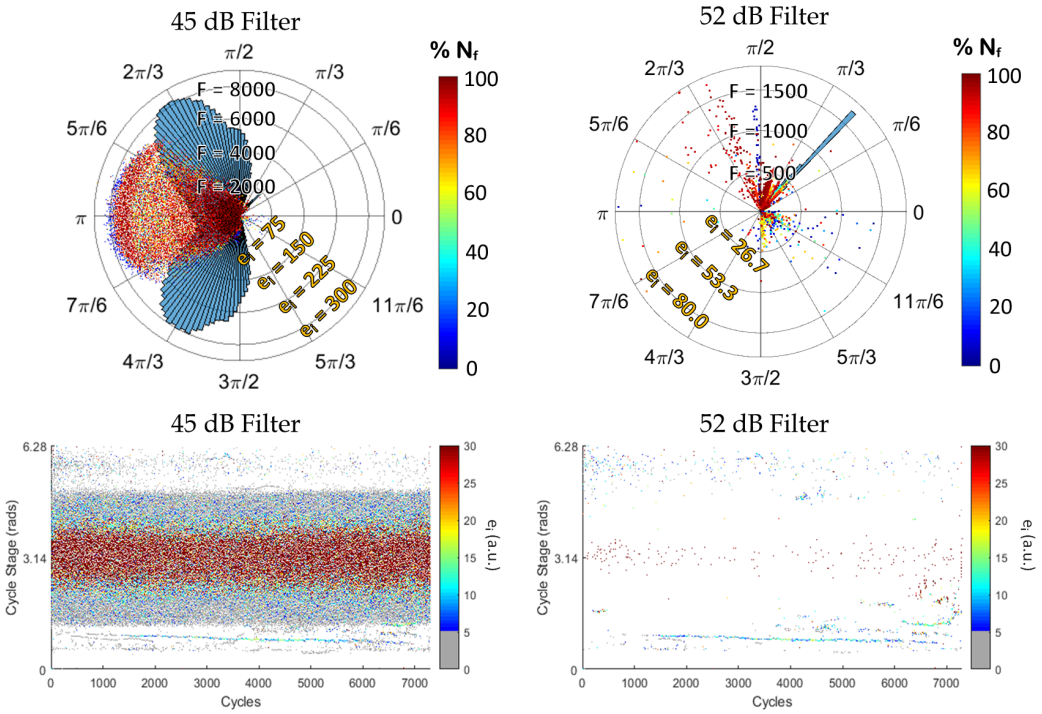

Figure 35: The cycle stage of hits measured during fatigue crack growth of Sample 1 presented as a polar graph (above) and against cycles (below) with an amplitude filter of 45 dB and 52 dB (left and right respectively).

R260 samples. In all samples, most hits occurred between $\frac{\pi}{6}$ and $\frac{\pi}{2}$ radians corresponding to 16% and 55% of P_{Max} on loading. This was similar to the timing of hits measured during the testing of the Hadfield steel samples, although it is a larger range. As these hits occurred during loading, it is likely that they were related to crack propagation or friction of the crack surfaces as it opened.

In half of the samples (4, 6, 8, 9 and 10) relatively high energy hits were consistently measured at around $\frac{5\pi}{3}$ radians (33% of P_{Max} on unloading). It is likely that these events were related to crack closure. This suggests that the fatigue cracks were closing at a very consistent force value (during unloading) across these samples.

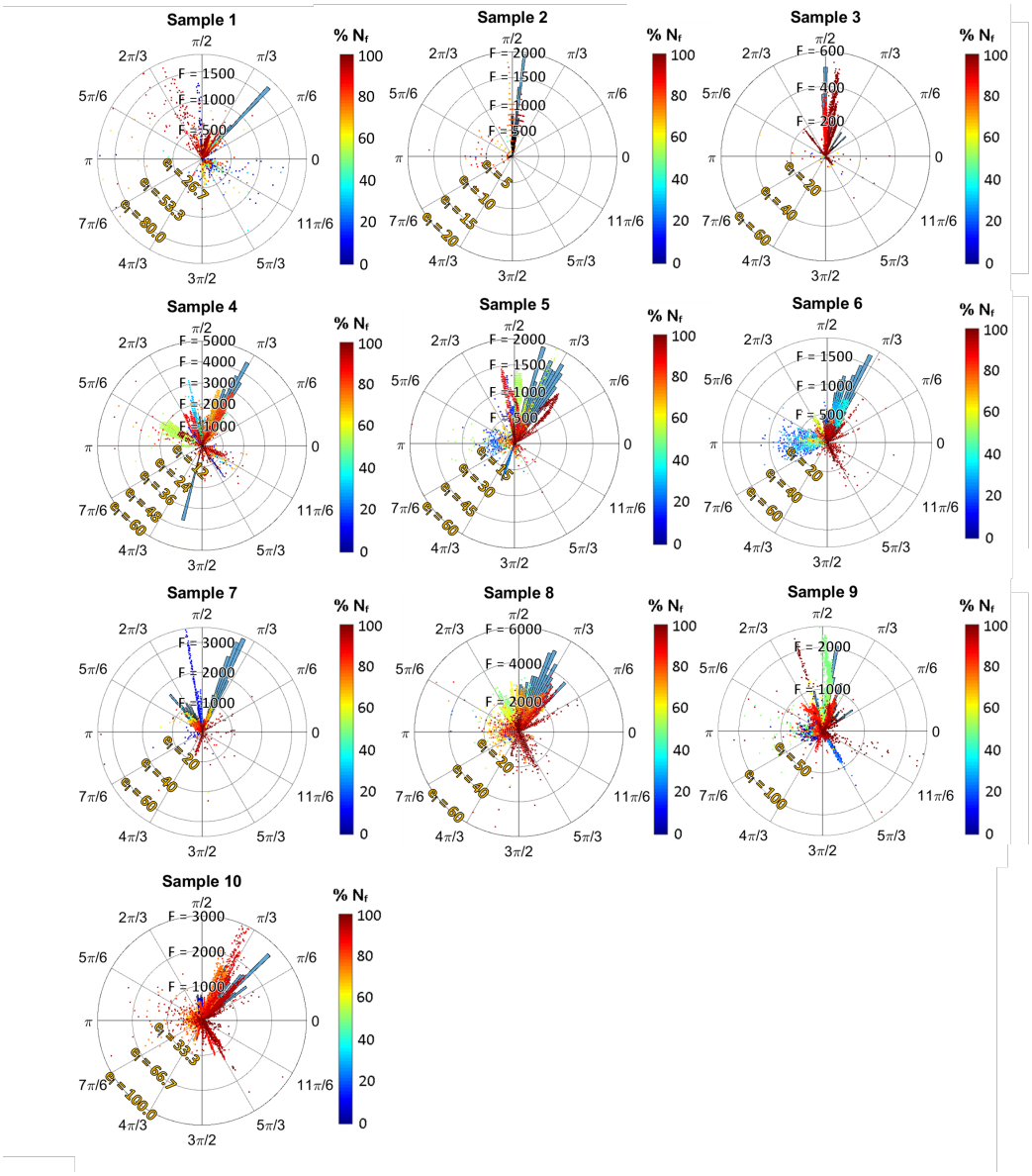

Figure 36: Polar scatter plots (e_i is hit energy) and histogram bars (F is frequency) of the cycle stage at which events were measured as R260 rail steel samples underwent fatigue loading.

Figure 37 shows how the cycle stage that hits were measured changed as the cracks grew. Energy values below 5 a.u. have been coloured grey for better comparison with the Hadfield steel data in Figure 26. In some samples, there are sudden changes in the hit timing which can be explained by the test being paused and resumed. For example, in sample 3 there was less noise measured at π radians after around 21,000 cycles. Generally, the majority of AE activity was measured during loading. Lines can be observed for AE hits which were measured at a very similar cycle stage over many cycles, typically trending downwards. This suggests that the events causing these hits occurred at a slightly earlier time each cycle as the crack grew.

For AE hits measured on unloading (therefore likely to be caused by crack closure) the stage in the cycle at which they occurred did not appear to change, with any trend lines being horizontal. These lines appear as peaks in the unloading stage of the polar histograms in Figure 36.

Amplitude

The amplitude of the AE throughout the test on each R260 steel sample is shown in Figure 38. It can be observed that the measured amplitude typically showed a general increase as the crack progressed, and that immediately prior to failure there were some very high amplitude hits in all samples, which acted as alarms of imminent failure. However, there were also a few high amplitude hits measured earlier, often when the crack had grown to around half of its final length (samples 3, 4, 6, 8, 9 and 10). For samples 3, 9 and 10, the time at which these high amplitude hits were measured (22,000, 49,500

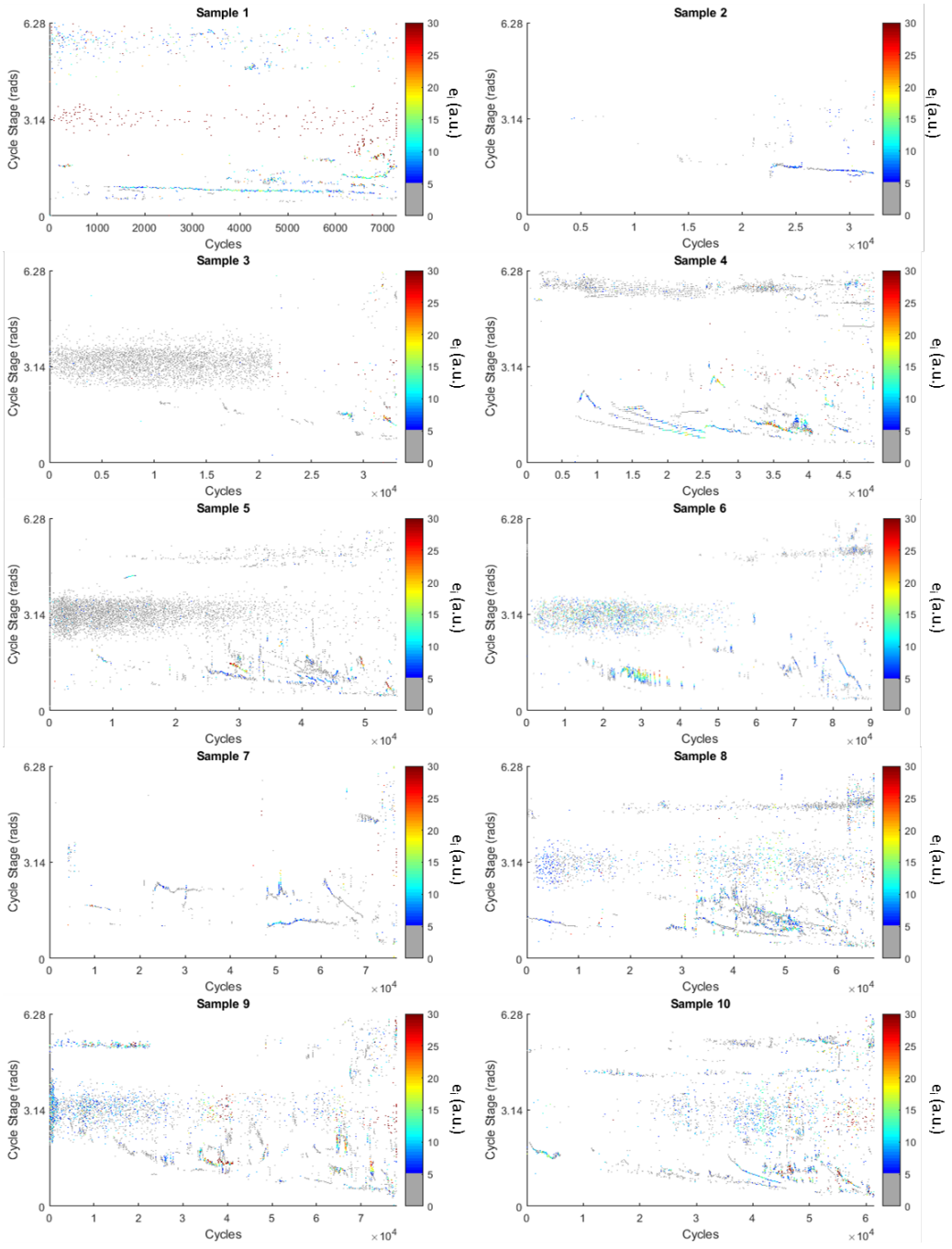

Figure 37: Hit graphs of ten R260 steel samples. The color of each data point represents the energy.

and 29,500 respectively) matched the change in crack growth to its region 2 (Paris's Law) growth phase identified in [14] (at respective ΔK values of 17.93, 19.53, and 19.06). This can most clearly be seen in sample 3 by the clear change in the gradient of crack growth that occurred at 22,000 cycles in Figure (38).

The most sudden change in crack growth was seen at around 70,000 cycles in sample 7. However, there was no significant corresponding change in the AE amplitudes measured at this point. The AE amplitude can therefore be used to give an indication of changes to the crack growth, but it cannot necessarily be relied upon.

Similarly to the Hadfield samples, a decrease in the amplitude of measured AE can be seen leading up to the failure of multiple R260 samples. This is likely to be due to plasticity at the crack tip.

Analysis of $\frac{da}{dN}$, $\frac{dC_P}{dN}$, $\frac{dE_P}{dN}$, with ΔK and Cumulative Counts and Energy with Crack Length

Analysis of the relationships between $\frac{da}{dN}$, $\frac{dC_P}{dN}$ and $\frac{dE_P}{dN}$ with ΔK along with cumulative counts and energy with the crack length for these samples can be found in reference [14].

4.2 Model of Crack Propagation through Rail Steel containing an Inclusion

The stress within the model before and after the crack severed the inclusion can be seen in Figure 39. Prior to being reached by the crack tip, the

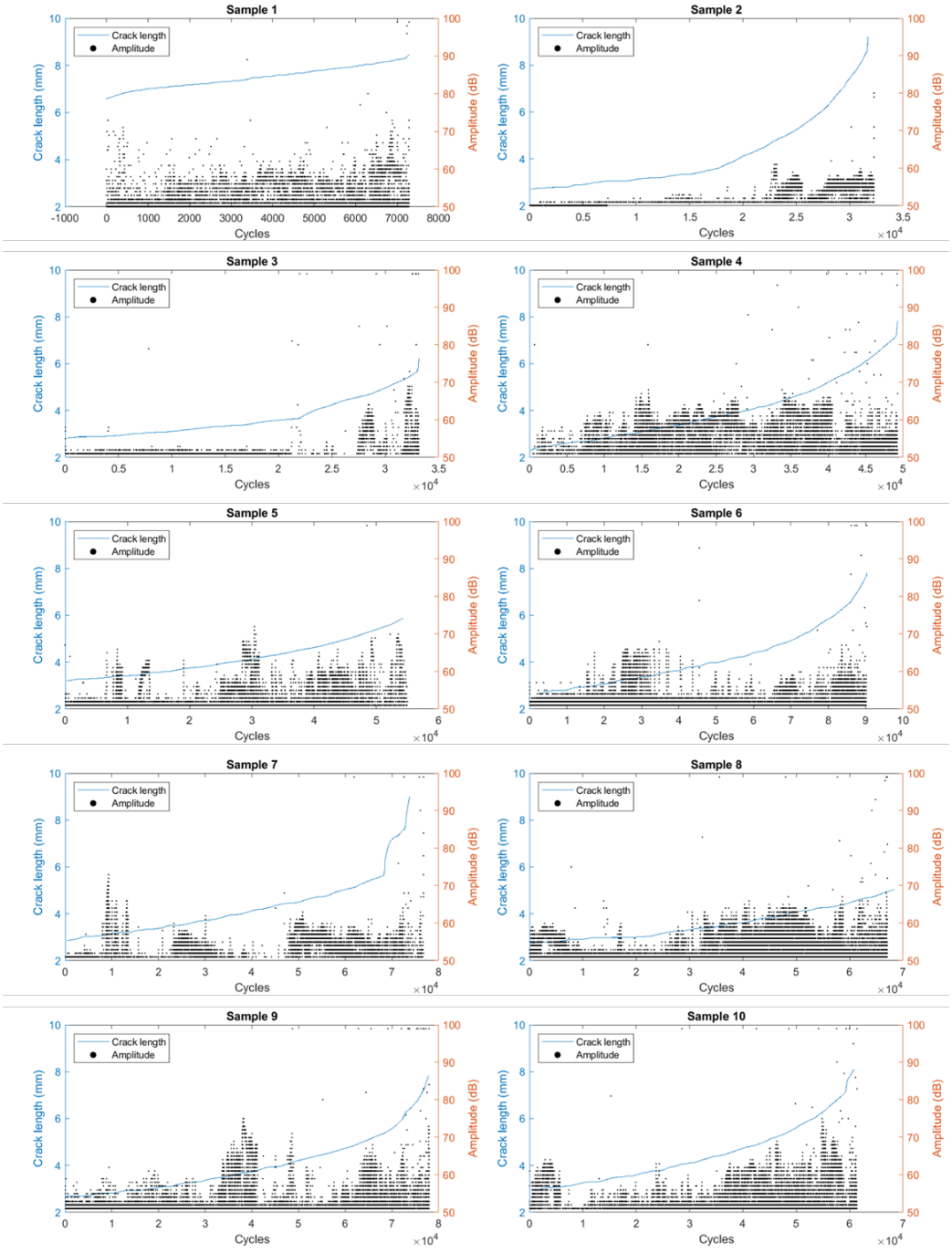

Figure 38: Amplitude of the AE signal for ten R260 samples with the crack length also shown.

inclusion can be seen to experience a much higher stress than the surrounding matrix. This is because of the difference between the plastic properties of the matrix (which resulted in plastic deformation) and the elastic properties of the inclusion (where the stress could continue to increase as the elastic strain increased).

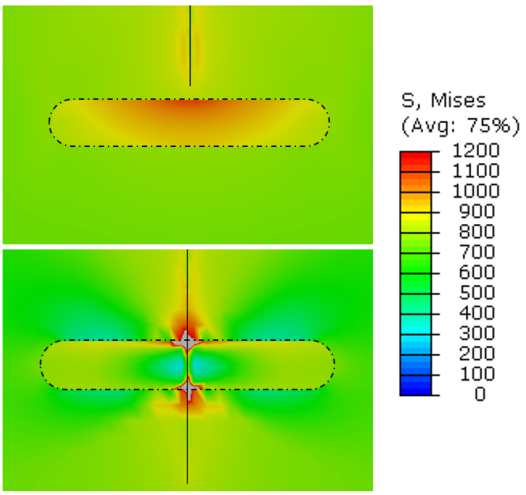

Figure 39: The Von Mises plot of the area around the inclusion (outlined) as the crack approached at 0.48 s (above) and after it had been severed by the crack (below).

The crack grew straight as shown in Figure 39 which was expected due to the symmetry in the model. The length of the modelled crack as a function of time is shown in Figure 40. It can be seen that when the crack reached the inclusion its growth rapidly increased. The step increase in crack length also continued past the inclusion.

The energy that was released throughout the simulation can be seen in Figure 41. There was a significant step in ALLDMD at the same point that there was a step in the crack length (see Figure 40). This makes sense as ALLDMD is proportional to crack length for a given material and although

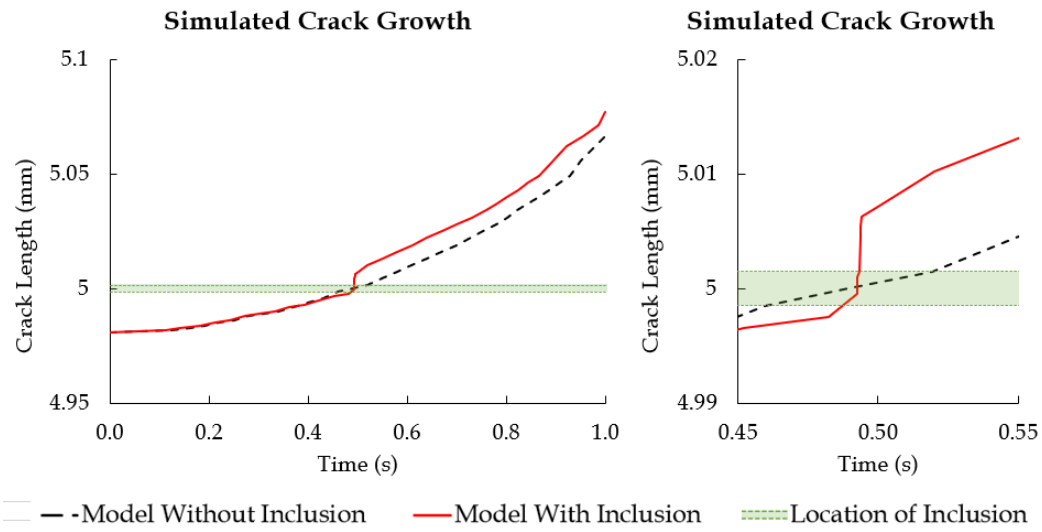

Figure 40: The crack length over the simulation with and without an inclusion present. The location of the inclusion along the crack front has been highlighted.

the fracture energy was much smaller for the soft sulphide inclusion than the R260 matrix, the fast crack propagation extended past the inclusion into the matrix. After this point, the crack continued to grow at a faster rate than the crack in the matrix without the inclusion. This is because the crack was longer, resulting in a higher stress intensity factor for each given point in time.

In contrast, ALLPD was very similar for both simulations. A small step can be observed at the point where the rapid crack growth occurred, but it is insignificant in magnitude. This suggests that the plastic response of the matrix was influenced by the applied bending (as a result of the ramp displacement) to the extent that any influence from the crack length was almost insignificant.

The graph of ALLDMD and ALLPD combined (see Figure 41) appears

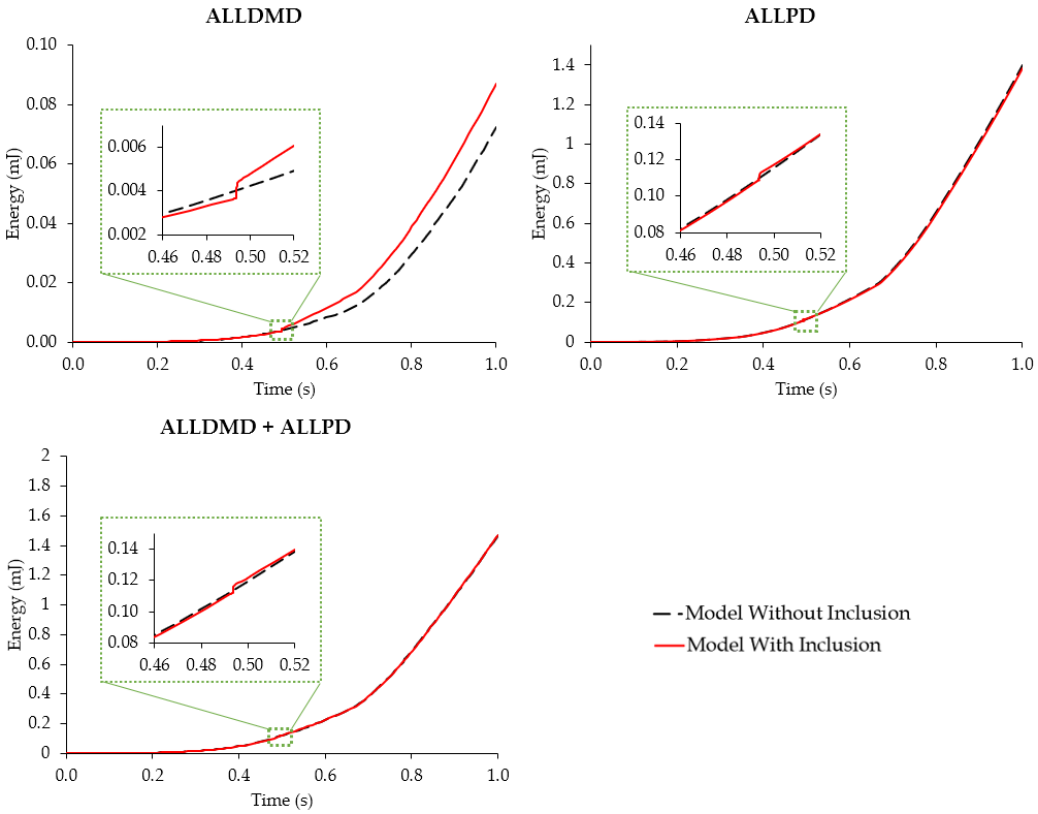

Figure 41: Energy released due to crack growth (ALLDMD) and plastic deformation (ALLPD) as a simulated crack grew through a sample with and without a soft sulphide inclusion present. Energy values are per 1 μm thickness.

very similar to the ALLPD graph. This is because of the much larger magnitude of ALLPD values than ALLDMD values. In theory, this might mean that measurement of energy during a similar practical experiment could easily miss such a step in energy. However, in the case of AE inspection the technique is thought to be incapable of measuring typical plasticity in steel [63]. The ALLDMD plot is therefore more likely to represent what would be measured during AE inspection than the ALLPD plot or their combination.

Data from around the point marked "(f)" in [12] is shown in Figure

42. The crack was measured with DCPD which resulted in a much lower resolution than could be achieved in the simulation. For this reason it could not be used to confirm whether there was a rapid increase in the crack length at the time that the step in cumulative energy was measured.

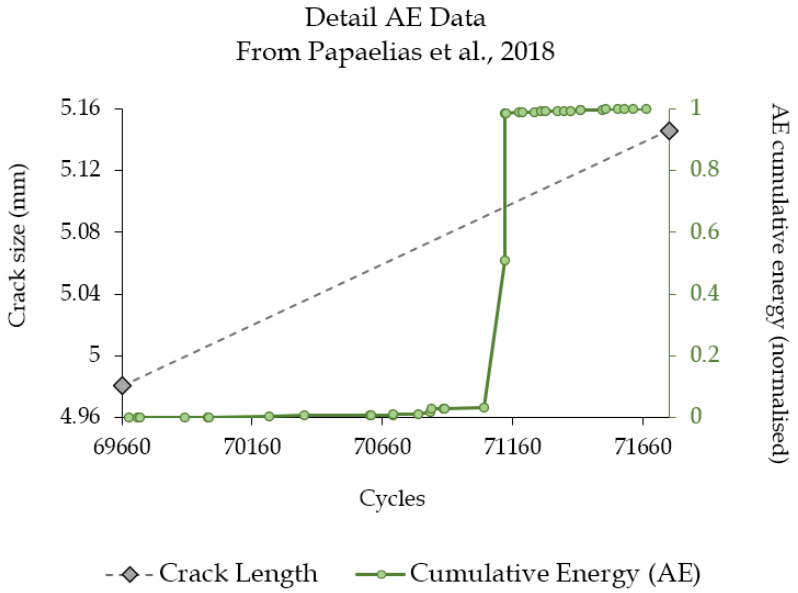

Figure 42: Crack length and AE energy (normalised) as a fatigue crack propagated near to and through an inclusion [12].

Over the 2000 cycles shown, fatigue crack growth was occurring in the sample (using linear interpolation the average growth per cycle can be estimated at around 0.082 μm). If the AE consisted only of signals relating to crack growth and no data was lost (e.g. through filtering or attenuation), steady crack growth through a homogeneous medium would be expected to result in a proportional increase in the energy measured through G_{IC}. Over the range shown in Figure 42, this would equate to an energy release of around 6.1 $\mu J/cycle$ (0.61 $\mu J/cycle$ per mm thickness). However, it can be observed that very little energy was measured by the AE sensor aside from

the step increase. This suggests that the incremental fatigue crack growth did not produce enough energy to be measured, and that something different occurred at the point at which the step was measured. This could have been due to more severe crack growth occurring, or a sudden AE event of a different type being measured (e.g. friction, crack closure or noise). As an inclusion was found on the surface at the location that the location corresponding to the step, it is likely that similarly to the model the step in energy was a result of instantaneous acceleration in crack propagation caused by the presence of some kind of inclusion.

In the physical experiment performed in this project and analysed earlier in this chapter and in reference [14], it was observed that cumulative AE energy increased in a step-wise motion in both Hadfield steel and R260 steel. These modelling results suggest that some of the step increases in cumulative energy could have been the result of fast crack propagation due to the presence of an inclusion at those points.

Limitations

The following limitations should be considered when interpreting the results and comparing them to the conditions that resulted in a step in cumulative AE in [12]:

- In the physical experiment, cyclic loading was applied and the crack grew due to fatigue. In the FEA, crack growth occurred as a result of a linear displacement of the top pin. The crack growth mechanisms would therefore differ.

- A two-dimensional model was used meaning that the results were given per 1 μm thickness. In three dimensions the crack growth would likely vary along the thickness of the crack front as the crack met an inclusion as inclusions in rail steel are not through-thickness. As a result, the proportional energy release as an inclusion causes fast crack propagation may be less distinctive than the step seen in Figure 41.

5 CONCLUSIONS AND FUTURE WORK

5.1 Conclusions

The increasing demand for rail travel means that it is valuable to come up with new solutions for inspection and maintenance that are less disruptive and raise lifecycle efficiency. The environmental conditions, loading and material inhomogeneity of rails can make defects difficult to predict. It is therefore important to monitor rail health and to develop models to further understand how, why, and when they fail.

Acoustic emission (AE) is an established technology for passive inspection. It has previously been shown to be capable of assessing structural health as well as detection, location and quantification of fatigue crack initiation and growth. Previous work has shown that cracks can be quantified within rail steel using AE, albeit for a simple crack in laboratory testing conditions where noise is much lower than in rail application.

Cast manganese steel (otherwise known as Hadfield steel) is used at rail crossings where its excellent properties and propensity to work harden make it ideal for handling the tougher conditions such as frequent impact loads. The quantification of cracks in Hadfield steel using AE has not previously been achieved. In this work, quantification of cracks in Hadfield steel using the count rate was investigated. The findings were the same as those in similar works and the count rate and energy rate of AE showed no apparent relationship to the stress intensity factor. Therefore, although the cracks adhered to Paris's growth behaviour, the count rate and energy rate could not be linked to the crack growth rate. This suggests that techniques that

have previously been used to quantify crack growth within pearlitic rail steel (used for the majority of sections of rail) cannot be applied to quantify cracks within Hadfield steel (used for rail crossings).

In a three-point bending fatigue test of steel where $R < 0.45$, the measured AE is expected to be a result of crack propagation and friction between the crack surfaces as they open and close. This work looked at the cycle stage at which hits were measured, investigating times at which higher energy hits were measured, times that hits were most frequently measured, and trends in how the cycle stage at which hits were measured changed over time. Additionally, a demonstration was given on how analysing visually the cycle stage can aid in noise removal and its validation.

It was found that for both Hadfield steel and R260 steel, hits were most frequently measured during the loading stage at between 33% and 55% of the maximum force. This suggests that the AE passing the filters was primarily a result of crack propagation and/or friction during crack opening. It was also observed that the hits were measured at a similar time from cycle-to-cycle but slightly earlier each time in both steels, suggesting that the event causing the AE release occurred at an earlier point as the crack grew. This could be due to larger cracks requiring less force to propagate, and the crack opening at an earlier stage. In contrast, crack closure events were identified to typically occur at the same time each cycle when measured suggesting that the crack closed at the same point in each cycle regardless of the crack length.

Cycle stage analysis was only possible because the frequency of the test was constant and known. During use, rails are exposed to stochastic loads

and the time of AE measurement with regards to maximum load would be difficult to pinpoint. Therefore, to characterise event types requires different approaches such as looking at the AE waveform (e.g. Figure 28) or by using the frequency domain as demonstrated by Li et al. [11].

High amplitude hits immediately prior to failure were observed in all R260 steel samples, but only 20% of the Hadfield steel samples. In some R260 steel samples this additionally occurred immediately before the crack began to enter its Paris's law behaviour of growth. This suggests that in the main part of the rail, high amplitude hits can be used as an indication of change in crack growth behaviour or an alarm of imminent failure. In crossings this warning might not be possible to rely upon as a final warning before failure. However, for safety reasons it is imperative to avoid damage to this point in rails so the application of this knowledge is limited.

Analysis of cumulative counts and energy showed similar step-wise type trends in the data to those observed in the literature. These can be used to help assess the length of the crack, but the variety of magnitudes that these values reached before failure makes this difficult.

Previously, steps in cumulative energy have been associated with the point at which an inclusion was cracked within the matrix. It was shown using Finite Element Analysis (FEA) that as a crack reached a soft manganese sulphide inclusion, rapid crack growth was caused along with a resultant sudden increase in energy released. This supported the previous suggestion that these steps in AE energy can be a result of present inclusions causing fast crack propagation.

Modelling of rails has advanced significantly in the past decade, with

research being done on both the general response of the material to cyclic loading as well as full geometrical models which incorporate the wheel-rail interaction. However, there are some limitations to these models such as the missing consideration of residual stresses introduced through manufacture and use as well as the different hardening behaviours exhibited at different head depths [6]. Although links have been made between FEA and AE (including in this work), a model does not yet exist, to the author's knowledge, that translates AE data into damage or crack growth.

5.2 Future Work

The AE-monitored TPB test should be repeated with work-hardened Hadfield steel samples, as this would reduce plastic deformation during precracking and fatigue crack growth. The crack would grow and release AE signals in a fashion closer to what would be expected in application, as the surface of crossings are work hardened for most (if not all) of their life. The count rate and energy rate should then be compared with the stress intensity factor range and, if a relationship is observed, quantification of the crack growth should be attempted. The amplitude should also be compared with time and crack length to see if high amplitude hits occur immediately prior to failure across all samples.

Further work should also be done into modelling rails. The behaviour of rail steel is complex due to its inhomogeneities. Further material models should be developed to better represent the difference in properties and hardening behaviour that has been observed along the depth from the surface of

the rail head.

The creation of an accurate, fully functional digital twin for rail using inputs from AE sensors is very desirable as an economic solution to the challenges faced by rail inspection. It would mean that the active inspection methods that are currently used would only be required for validation, vastly reducing the amount of time over which the rails must be closed. The detection capability of AE would also mean that defects could be caught early and simple corrective maintenance (such as grinding) could be performed to avoid more disruptive maintenance being required at a later point.

To achieve this, the material behaviour of rail steel must be fully understood and reproduced in a model. AE cannot provide information on steel plasticity, so to include this within the model it must be reproduced using mechanical based FEA. The model must then be able to take AE data and translate it into crack data. If a single crack was present this could be a case of relating the AE parameter rates to the stress intensity factor range and translating into estimated crack growth. The direction of crack growth could in part be determined by the location data of the AE, but also informed by the distribution of stresses within the model as a load is applied. This load could also be an accurate reproduction of the loads exerted by passing rolling stock if they were measured near to the sensor.

In rails, the most common type of crack is caused by Rolling Contact Fatigue (RCF). These are typically initiated in clusters. Research should therefore also be performed into the location and quantification of cracks within these clusters.

Models of specific events (such as the cracking of the soft sulphide inclu-

sion which was presented in this work) could also be developed so that the relationship between AE and FEA can be better defined. Pattern recognition between physical deformation with AE and simulated deformation with theoretical energy release could provide better representation of deformation during particular scenarios. It would also reduce the processing required by enabling interpretation of AE as an input rather than each individual AE event.

For this form of inspection to be feasible over the long lifetime of rails, the AE data must be handled appropriately. Similarly to this report, parametric data should be used and events that do not contain significant AE (such as low energy events) should be discarded in order to reduce the size of the data. In addition, a sensor could be used to detect the approach of rolling stock and AE could be exclusively measured as it is loaded to reduce processing requirements and noise. Systems should also be set up to wirelessly transmit the data so that the simulations could be performed remotely without requiring rail access.

References

[1] Department for Transport. National travel survey: 2020. Technical report, September 2021. URL https://www.gov.uk/government/statistics/national-travel-survey-2020/national-travel-survey-2020.

[2] D. Y. Jeong and O. Orringer. Fatigue crack growth of surface cracks in the rail web. *Theoretical and Applied Fracture Mechanics*, 12(1):45–58, October 1989. doi: 10.1016/0167-8442(89)90014-1.

[3] K. Doraci and A. Hasanaj. The optimising force balance exercised in the wheel - profile contact force during the curved path. an experimental approach of using curvilinear profiles. pages 300–303, January 2017. doi: 10.21175/RadProc.2017.60.

[4] Farrat favim - used as sub-ballast rail isolation, 2022. URL https://farrat.com/anti-vibration-materials-washers-bushes/favim-fv10/favim-used-as-sub-ballast-rail-isolation. [Online; accessed 01-June-2022].

[5] V. Luzin, H. Prask, T. Gnäupel-Herold, J. Gordon, D. Wexler, C. Rathod, S. Pal, W. Daniel, and A. Atrens. Neutron residual stress measurements in rails. *Neutron News*, 24:307–314, July 2013. doi: 10.1080/10448632.2013.804353.

[6] A. C. Athukorala, D. V. De Pellegrin, and K. I. Kourousis. Characterisation of head-hardened rail steel in terms of cyclic plasticity response and microstructure for improved material modelling. *Wear*, 366-367: 416–424, April 2016. doi: 10.1016/j.wear.2016.03.024.

[7] What is points and crossing in railway engineering?, 2015. URL https://yamannvinci069.blogspot.com/2015/09/what-is-points-and-crossing-in-railway.html. [Online; accessed 30-March-2022].

[8] G. Thomson. Rail line damage repairs progress after barnawartha derailment. *The Guardian*. URL https://www.bordermail.com.au/story/6609815/rail-line-damage-repairs-progress-after-barnawartha-derailment/. [Online; accessed 30-March-2022].

[9] A. Ekberg, E. Kabo, J. Nielsen, and J. Ringsberg. Researchers on the track of wheel-rail interaction. *Railway gazette international*, 159(6): 397, June 2003.

[10] W. Sikorski. Active dielectric window: A new concept of combined acoustic emission and electromagnetic partial discharge detector for power transformers. *Energies*, 12(1), December 2019. doi: 10.3390/en12010115.

[11] D. Li, K. S. C. Kuang, and C. G. Koh. Fatigue crack sizing in rail steel using crack closure-induced acoustic emission waves. *Measurement Science and Technology*, 28(6):065601, April 2017. doi: 10.1088/1361-6501/aa670d.

[12] M. Papaelias, A. Amini, R. Culwick, J. Heesom, Z. Huang, V. Jantara, S. Kaewunruen, S. Kerkyras, M. Kongpuang, F. Marquez, S. Shi, A. Upton, and P. Vallely. Advanced remote condition monitoring of railway infrastructure and rolling stock. *1st International Conference on Welding and Non-Destructive Testing*, October 2018.

[13] A. Vinogradov and I. S. Yasnikov. On the nature of acoustic emission and internal friction during cyclic deformation of metals. *Acta materialia*, 70:8–18, May 2014. doi: 10.1016/j.actamat.2014.02.007.

[14] J. Payne. Remote conditioning monitoring of rails. Master's thesis, University of Birmingham, September 2020.

[15] R. Culwick. Remote conditioning monitoring of railway assets. Master's thesis, University of Birmingham, March 2019.

[16] A. Consilvio, A. Di Febbraro, and N. Sacco. A modular model to schedule predictive railway maintenance operations. In *International Conference on Models and Technologies for Intelligent Transportation Systems*, pages 426–433, June 2015. doi: 10.1109/MTITS.2015.7223290.

[17] Corus Group plc. Characterisation of microstructural deformation as a function of rail grade. Technical report, November 2009. URL `https://www.charmec.chalmers.se/innotrack/deliverables/sp4/d436-f3-microstructural_deformation_as_a_function_of_rail_grade.pdf`.

[18] Australian Rail Track Corporation Ltd. Technical specification for manufacture of components for points & crossing structures. Technical report, March 2008. URL `https://academia.edu/41983959/ETA_03_03_Technical_Specification_for_Points_and_Crossing`.

[19] R. Culwick, J. Payne, V. Jantara Junior, S. Roshanmanesh, and M. Papaelias. Advancements in acoustic emission monitoring techniques. *Manuscript submitted for publication*, 2022.

[20] S. Maya-Johnson, A. J. Ramirez, and A. Toro. Fatigue crack growth rate of two pearlitic rail steels. *Engineering fracture mechanics*, 138: 63–72, March 2015. doi: 10.1016/j.engfracmech.2015.03.023.

[21] J. T. Maximov, G. V. Duncheva, I. M. Amudjev, A. P. Anchev, and N. Ganev. A new approach for pre-stressing of rail-end-bolt holes. *Proceedings of the Institution of Mechanical Engineers, Part C: Journal of Mechanical Engineering Science*, 231(12):2275–2283, February 2016. doi: 10.1177/0954406216630003.

[22] L. Chen. Study on the effects of ti micro-addition on the characteristics of MnS inclusions in rail steel. *Ironmaking & Steelmaking*, 46(6):508–512, December 2017. doi: 10.1080/03019233.2017.1405177.

[23] P. Matteis and R. Sesana. Some comments on mechanical fatigue characterization of steel rails in standards. *Procedia Structural Integrity*, 3: 459–467, May 2017. doi: 10.1016/j.prostr.2017.04.064.

[24] K. Persson. Materials data on MnS (sg:216) by materials project, 2016. URL `https://materialsproject.org/materials/mp-1783/`.

[25] Hellma Materials. CVD zinc sulfide - Cleartran, January 2020. URL `https://hellma.com/en/crystalline-materials/optical-materials/cvd-zinc-sulfide-and-cleartran/`. [Online; accessed 25-March-2021].

[26] A. Davies. Handbook of condition monitoring : techniques and methodology, 1998.

[27] Network Rail. Broken rail, 2021. URL `https://www.networkrail.co.uk/running-the-railway/looking-after-the-railway/delays-explained/broken-rail/`. [Online; accessed 01-June-2022].

[28] Office of Rail Regulation. Train derailment at Hatfield: A final report by the independent investigation board. Technical report, Office of Rail Regulation, July 2006.

[29] Hatfield crash 'was disaster waiting to happen'. *The Telegraph*, January 2005. URL `www.telegraph.co.uk/news/1482439/Hatfield-crash-was-disaster-waiting-to-happen.html`. [Online; accessed 30-June-2022].

[30] Press Association. How Hatfield changed the rail industry. *The Guardian*, September 2005. URL `www.theguardian.com/uk/2005/sep/06/hatfield.transport`. [Online; accessed 30-June-2022].

[31] J. Kelleher, M. Prime, D. Buttle, P. Mummery, P. Webster, J. Shackleton, and P. Withers. The measurement of residual stress in railway rails by diffraction and other methods. *Journal of Neutron Research*, 11:187–193, December 2003. doi: 10.1080/10238160410001726602.

[32] F. P. L. Kavishe and T. J. Baker. Effect of prior austenite grain size and pearlite interlamellar spacing on strength and fracture toughness of a eutectoid rail steel. *Materials Science and Technology*, 2(8):816–822, July 1986. doi: 10.1179/mst.1986.2.8.816.

[33] J.E. Garnham and C.L. Davis. *5 - Rail materials*. Woodhead Publishing, 2009. doi: 10.1533/9781845696788.1.125.

[34] S. Mikheevskiy, S. Bogdanov, and G. Glinka. Analysis of fatigue crack growth under spectrum loading – the unigrow fatigue crack growth model. *Theoretical and Applied Fracture Mechanics*, 79:25–33, October 2015. doi: 10.1016/j.tafmec.2015.06.010.

[35] J. Kalousek and A. E. Bethune. Rail wear under heavy traffic conditions. pages 63–79, January 1978. doi: 10.1520/STP27103S.

[36] E. V. Iarve, K. Hoos, M. Braginsky, E. Zhou, and D. H. Mollenhauer. Progressive failure simulation in laminated composites under fatigue loading by using discrete damage modeling. *Journal of Composite Materials*, 51(15):2143–2161, June 2017. doi: 10.1177/0021998316681831.

[37] B. Bramfitt, R. Steele, and J. Martens. *Rail Steels—Developments, Manufacturing and Performance*. ISS, Warrendale, PA, 1993.

[38] G. Bhavani, J. Srivastava, and V. Mahesh. Characterization of used and virgin pearlitic rail steel. *Materials Today: Proceedings*, 39:454–458, September 2020. doi: 10.1016/j.matpr.2020.07.718.

[39] G. Tęcza and S. Sobula. Effect of heat treatment on change microstructure of cast high-manganese Hadfield steel with elevated chromium content. *Archives of Foundry Engineering*, 14:67–70, October 2014.

[40] A. Srivastava. Microstructural characterization of hadfield austenitic manganese steel. *Journal of Materials Science*, 43:5654–5658, January 2008. doi: 10.1007/s10853-008-2759-y.

[41] E.G. Moghaddam, Nasser Varahram, and P. Davami. On the comparison of microstructural characteristics and mechanical properties of high-vanadium austenitic manganese steels with the hadfield steel. *Materials Science and Engineering A-structural Materials Properties Microstructure and Processing*, 532:260–266, January 2012. doi: 10.1016/j.msea.2011.10.089.

[42] I. Karaman, H. Sehitoglu, Yury Chumlyakov, H. Maier, and I. Kireeva. Extrinsic stacking faults and twinning in hadfield manganese steel single crystals. *Scripta Materialia*, 44:337–343, February 2001. doi: 10.1016/S1359-6462(00)00600-X.

[43] P. Havlicek and P. Nesvadba. Application of explosive hardening on railway infrastructure parts. In *Metal 2011*, May 2011.

[44] G. Mi, H. Nan, Y. Liu, B. Zhang, H. Zhang, and G. Song. Influence of inclusion on crack initiation in wheel rim. *Journal of Iron and Steel Research, International*, 18(1):49–54, January 2011. doi: 10.1016/S1006-706X(11)60010-1.

[45] J. Qi, W. Zhu, C. Yang, T. Ou, J. Chen, and Y. Liu. MnS inclusion behavior in heavy rail steel during heating process. *Heat Treatment of Metals*, 38:40–42, June 2013.

[46] D.M. Fegredo, M.T. Shehata, A. Palmer, and J. Kalousek. The effect of sulphide and oxide inclusions on the wear rates of a standard C-Mn and a Cr-Mo alloy rail steel. *Wear*, 126(3):285–306, September 1988. ISSN 0043-1648. doi: 10.1016/0043-1648(88)90171-8.

[47] W. Ren, L. Wang, Z. Xue, C. Li, H. Zhu, A. Huang, and C. Li. A thermodynamic assessment of precipitation, growth, and control of MnS inclusion in U75V heavy rail steel. *High temperature materials and processes*, 40(1):178–192, June 2021. doi: 10.1515/htmp-2021-0022.

[48] J. Bian, Y. Gu, and M. H. Murray. A dynamic wheel-rail impact analysis of railway track under wheel flat by finite element analysis. *Vehicle system dynamics*, 51(6):784–797, March 2013. doi: 10.1080/00423114.2013.774031.

[49] C. L. Pun, Q. Kan, P. J. Mutton, G. K., and W. Yan. Ratcheting behaviour of high strength rail steels under bi-axial compression–torsion loadings: Experiment and simulation. *International Journal of Fatigue*, 66:138–154, March 2014. doi: 10.1016/j.ijfatigue.2014.03.021.

[50] A. F. Bower and K. L. Johnson. Plastic flow and shakedown of the rail surface in repeated wheel-rail contact. *Wear*, 144(1):1–18, April 1991. doi: 10.1016/0043-1648(91)90003-D.

[51] S. Bogdański, J. Stupnicki, M. W. Brown, and D. F. Cannon. A two dimensional analysis of mixed-mode rolling contact fatigue crack growth in rails. *European Structural Integrity Society*, 25:235–248, January 1999. doi: 10.1016/S1566-1369(99)80018-1.

[52] J. Brouzoulis and M. Ekh. Crack propagation in rails under rolling contact fatigue loading conditions based on material forces. *International Journal of Fatigue*, 45:98–105, December 2012. doi: 10.1016/j.ijfatigue.2012.06.002.

[53] L. F. Kawashita and S. R. Hallett. A crack tip tracking algorithm for cohesive interface element analysis of fatigue delamination propagation in composite materials. *International Journal of Solids and Structures*, 49(21):2898–2913, October 2012. doi: 10.1016/j.ijsolstr.2012.03.034.

[54] J. Garnham, F. J. Franklin, D. I. Fletcher, A. Kapoor, and C. Davis. Predicting the life of steel rails. *Proceedings of the Institution of Mechanical Engineers Part F Journal of Rail and Rapid Transit*, 221(1): 45–58, January 2007. doi: 10.1243/09544097JRRT66.

[55] X. Feng, F. Zhang, C. Zheng, and L. Bo. Micromechanics behavior of fatigue cracks in hadfield steel railway crossing. *Science China Technological Sciences*, 56:1151–1154, April 2013. doi: 10.1007/s11431-013-5181-x.

[56] W. Zhong, J.J. Hu, Z.B. Li, Q.Y. Liu, and Z.R. Zhou. A study of rolling contact fatigue crack growth in U75V and U71Mn rails. *Wear*, 271(1):388–392, May 2011. doi: 10.1016/j.wear.2010.10.071.

[57] S. Dhar, H. K. Danielsen, S. Fæster, C. Rasmussen, Y. Zhang, and D. Juul Jensen. Crack formation within a hadfield manganese steel crossing nose. *Wear*, 438-439:203049, November 2019. doi: 10.1016/j.wear.2019.203049.

[58] A. Ekberg and E. Kabo. Fatigue of railway wheels and rails under rolling contact and thermal loading—an overview. *Wear*, 258(7):1288–1300, March 2005. doi: 10.1016/j.wear.2004.03.039.

[59] Broken rail explained, 2022. URL https://www.networkrail.co.uk/stories/broken-rail-explained/. [Online; accessed 25-February-2022].

[60] J. E. Garnham, D. I. Fletcher, C. L. Davis, and F. J. Franklin. Visualization and modelling to understand rail rolling contact fatigue cracks in three dimensions. *Proceedings of the Institution of Mechanical Engineers, Part F: Journal of Rail and Rapid Transit*, 225(2):165–178, August 2011. doi: 10.1177/2041301710JRRT414.

[61] Planned works, 2021. URL www.networkrail.co.uk/running-the-railway/looking-after-the-railway/our-fleet-machines-and-vehicles. [Online; accessed 01-June-2022].

[62] M. Papaelias, C. Roberts, and C. L. Davis. A review on non-destructive evaluation of rails: State-of-the-art and future development. *Proceedings of the Institution of Mechanical Engineers, Part F: Journal of Rail and Rapid Transit*, 222(4):367–384, July 2008. doi: 10.1243/09544097JRRT209.

[63] D. G. Eitzen and H. N. G. Wadley. Acoustic emission: Establishing the fundamentals. *Journal of Research of the National Bureau of Standards*, 89(1):75, January 1984. doi: 10.6028/jres.089.008.

[64] M. N. Bassim, S. S. Lawrence, and C. D. Liu. Detection of the onset of fatigue crack growth in rail steels using acoustic emission. *Engineering Fracture Mechanics*, 47(2):207–214, January 1994. doi: 10.1016/0013-7944(94)90221-6.

[65] T. M. Roberts and M. Talebzadeh. Acoustic emission monitoring of fatigue crack propagation. *Journal of Constructional Steel Research*, 59(6):695–712, June 2003. doi: 10.1016/S0143-974X(02)00064-0.

[66] M. Akbari and M. Ahmadi. The application of acoustic emission technique to plastic deformation of low carbon steel. *Physics Procedia*, 3 (1):795–801, January 2010. doi: 10.1016/j.phpro.2010.01.102.

[67] A. Vinogradov, S. Hashimoto, and S. Miura. Effect of grain boundary on acoustic emission during plastic deformation of copper-aluminum bicrystals. *Acta Materialia*, 44(7):2883–2890, July 1996. doi: 10.1016/1359-6454(95)00375-4.

[68] M. Koslowski, R. Lesar, and R. Thomson. Avalanches and scaling in plastic deformation. *Physical review letters*, 93(12):125502, September 2004. doi: 10.1103/PhysRevLett.93.125502.

[69] J-B. Chung and E. Kannatey-Asibu. Acoustic emission from plastic deformation of a pure single crystal. *Journal of Applied Physics*, 72: 1812 – 1820, October 1992. doi: 10.1063/1.351652.

[70] M. Hrairi. Using acoustic emission and fractography to evaluate defects induced by corrosive environment. *Corrosion Engineering, Science and Technology*, 44(4):251–260, November 2009. doi: 10.1179/174327808X 303446.

[71] B. Omondi, D. G. Aggelis, H. Sol, and C. Sitters. Improved crack monitoring in structural concrete by combined acoustic emission and digital image correlation techniques. *Structural Health Monitoring*, 15 (3):359–378, May 2016. doi: 10.1177/1475921716636806.

[72] P. Vallely. *A holistic approach to remote condition monitoring for the accurate evaluation of railway infrastructure and rolling stock.* PhD thesis, University of Birmingham, July 2019.

[73] S. Shi. *Remote condition monitoring of structural integrity of rails and crossings using acoustic emission technique.* PhD thesis, University of Birmingham, July 2019.

[74] Z. Huang. *Integrated Railway Remote Condition Monitoring.* PhD thesis, University of Birmingham, December 2016.

[75] Q. Hao, K. Wang, Y. Wang, Y. Shen, X. Zhang, and H. Hu. An investigation on acoustic emission detection of rail crack in actual application by chaos theory with improved feature detection method. *Journal of Sound and Vibration*, 436(1):165–182, December 2018. doi: 10.1016/j.jsv.2018.09.014.

[76] Y. Rui, Z. Zhou, J. Lu, B. Ullah, and X. Cai. A novel AE source localization method using clustering detection to eliminate abnormal arrivals. *International Journal of Mining Science and Technology*, 32 (1):51–62, January 2022. doi: 10.1016/j.ijmst.2021.11.004.

[77] K. Bollas, D. Papasalouros, and A. Anastasopoulos. Acoustic emission inspection of rail wheels. *The e-Journal of Nondestructive Testing*, 17: 215–228, January 2012.

[78] F. Hamel, J. P. Bailon, and M. N. Bassim. Acoustic emission mechanisms during high-cycle fatigue. *Engineering Fracture Mechanics*, 14 (4):853–860, June 1981. doi: 10.1016/0013-7944(81)90097-7.

[79] T. C. Lindley, I. G. Palmer, and C. E. Richards. Acoustic emission monitoring of fatigue crack growth. *Materials Science and Engineering*, 32(1):1–15, January 1978. doi: 10.1016/0025-5416(78)90206-9.

[80] Z. F. Wang, J. Li, W. Ke, and Z. Zhu. Characteristics of acoustic emission for A537 structural steel during fatigue crack propagation. *Scripta Metallurgica et Materiala*, 27(5):641–646, July 1992. doi: 10.1016/0956-716X(92)90354-H.

[81] A. Berkovits and D. Fang. Study of fatigue crack characteristics by acoustic emission. *Engineering Fracture Mechanics*, 51(3):411–409, June 1995. doi: 10.1016/0013-7944(94)00274-L.

[82] T. M. Morton, R. M. Harrington, and J. G. Bjeletich. Acoustic emissions of fatigue crack growth. *Engineering Fracture Mechanics*, 5(3): 691–697, September 1973. doi: 10.1016/0013-7944(73)90047-7.

[83] D. Gagar, P. Foote, and P. Irving. A novel closure based approach for fatigue crack length estimation using the acoustic emission technique in structural health monitoring applications. *Smart Materials and Structures*, 23(12):105033, September 2014. doi: 10.1088/0964-1726/23/10/105033.

[84] S. Shi, Z. Han, Z. Liu, P. Vallely, S. Soua, S. Kaewunruen, and M. Papaelias. Quantitative monitoring of brittle fatigue crack growth in railway steel using acoustic emission. *Proceedings of the Institution of Mechanical Engineers, Part F: Journal of Rail and Rapid Transit*, 232 (4):1211–1224, April 2018. doi: 10.1177/0954409717711292.

[85] T. M. Roberts and M. Talebzadeh. Fatigue life prediction based on crack propagation and acoustic emission count rates. *Journal of Constructional Steel Research*, 59(6):679–694, June 2003. doi: 10.1016/S0143-974X(02)00065-2.

[86] M. Kongpuang, R. Culwick, N. Cheputeh, A. Marsh, V. Jantara Junior, P. Vallely, S. Kaewunruen, and M Papaelias. Quantitative analysis of the structural health of railway turnouts using the acoustic emission technique. *Insight - Non-Destructive Testing and Condition Monitoring*, 64:398–403, July 2022. doi: 10.1784/insi.2022.64.7.398.

[87] P. J. Singh, C. K. Mukhopadhyay, T. Jayakumar, S. L. Mannan, and B. Raj. Understanding fatigue crack propagation in AISI 316 (N) weld using Elber's crack closure concept: Experimental results from GC-MOD and acoustic emission techniques. *International Journal of Fatigue*, 29(12):2170–2179, December 2007. doi: 10.1016/j.ijfatigue.2006.12.013.

[88] R. Yuan and B. Shi. Acoustic emission activity in directly tensile test on marble specimens and its tensile damage constitutive model. *International journal of coal science and technology*, 5(3):295–304, September 2018. doi: 10.1007/s40789-018-0215-4.

[89] Z. T. Nazarchuk, V. Skalskyi, and O. Serhiyenko. *Acoustic emission: methodology and application*. Foundations of engineering mechanics. Springer, 2017. doi: 10.1007/978-3-319-49350-3.

[90] S. Bogdanski, M. Olzak, and J. Stupnicki. Numerical stress analysis of rail rolling contact fatigue cracks. *Wear*, 191(1):14–24, January 1996. doi: 10.1016/0043-1648(95)06685-3.

[91] S. Bogdański and M. W. Brown. Modelling the three-dimensional behaviour of shallow rolling contact fatigue cracks in rails. *Wear*, 253(1):17–25, July 2002. doi: 10.1016/S0043-1648(02)00078-9.

[92] D. Floros, A. Ekberg, and F. Larsson. Evaluation of mixed-mode crack growth direction criteria under rolling contact conditions. *Wear*, 448-449:203184, May 2020. doi: 10.1016/j.wear.2020.203184.

[93] D. Canadinc, H. Sehitoglu, and K. Verzal. Analysis of surface crack growth under rolling contact fatigue. *International Journal of Fatigue*, 30(9):1678–1689, September 2008. doi: 10.1016/j.ijfatigue.2007.11.002.

[94] J. E. Garnham and C. L. Davis. The role of deformed rail microstructure on rolling contact fatigue initiation. *Wear*, 265(9):1363–1372, October 2008. doi: 10.1016/j.wear.2008.02.042.

[95] N. Ohno and J-D. Wang. Kinematic hardening rules with critical state of dynamic recovery, part I: formulation and basic features for ratchetting behavior. *International Journal of Plasticity*, 9(3):375–390, August 1993. doi: 10.1016/0749-6419(93)90042-O.

[96] M. Abdel-Karim and N. Ohno. Kinematic hardening model suitable for ratcheting with steady-state. *International Journal of Plasticity*, 16:225–240, December 2000. doi: 10.1016/S0749-6419(99)00052-2.

[97] C. O. Frederick and P. J. Armstrong. A mathematical representation of the multiaxial bauschinger effect. *Materials at High Temperatures*, 24(1):1–26, January 2007. doi: 10.1179/096034007X207589.

[98] G. Kang and Q. Gao. Uniaxial and non-proportionally multiaxial ratcheting of U71Mn rail steel: experiments and simulations. *Mechanics of Materials*, 34(12):809–820, August 2002. doi: 10.1016/S0167-6636(02)00198-9.

[99] G. Kang. A visco-plastic constitutive model for ratcheting of cyclically stable materials and its finite element implementation. *Mechanics of Materials*, 36(4):299–312, April 2004. doi: 10.1016/S0167-6636(03)00024-3.

[100] K. A. Meyer. Evaluation of material models describing the evolution of plastic anisotropy in pearlitic steel. *International Journal of Solids and Structures*, 200:266–285, September 2020. doi: 10.1016/j.ijsolstr.2020.04.037.

[101] B. Shi, A. Bartels, and J. Mosler. On the thermodynamically consistent modeling of distortional hardening: A novel generalized framework. *International Journal of Plasticity*, 63:170–182, December 2014. doi: 10.1016/j.ijplas.2014.05.008.

[102] J. Qin, B. Holmedal, and O. S. Hopperstad. A combined isotropic, kinematic and distortional hardening model for aluminum and steels under complex strain-path changes. *International Journal of Plasticity*, 101:156–169, February 2018. doi: 10.1016/j.ijplas.2017.10.013.

[103] C. Miehe, J. Schröder, and J. Schotte. Computational homogenization analysis in finite plasticity simulation of texture development in polycrystalline materials. *Computer Methods in Applied Mechanics and Engineering*, 171(3):387–418, April 1999. doi: 10.1016/S0045-7825(98)00218-7.

[104] K. A. Meyer and A. Menzel. A distortional hardening model for finite plasticity. *International Journal of Solids and Structures*, 232:111055, April 2021. doi: 10.1016/j.ijsolstr.2021.111055.

[105] A. Esmaeili, J. Ahlstrom, B. Andersson, and M. Ekh. Modelling of cyclic plasticity and phase transformations during repeated local heating events in rail and wheel steels. *International Journal of Fatigue*, 151, October 2021. doi: 10.1016/j.ijfatigue.2021.106361.

[106] J. Lemaitre and J-L. Chaboche. *Mechanics of solid materials*. Cambridge university press, 1994.

[107] H. M. El-sayed, M. Lotfy, H. N. El din Zohny, and H. S. Riad. Prediction of fatigue crack initiation life in railheads using finite element analysis. *Ain Shams Engineering Journal*, 9(4):2329–2342, December 2018. doi: 10.1016/j.asej.2017.06.003.

[108] S. Bari and T. Hassan. Anatomy of coupled constitutive models for ratcheting simulation. *International Journal of Plasticity*, 16(3):381–409, February 2000. doi: 10.1016/S0749-6419(99)00059-5.

[109] S. Bari and T. Hassan. An advancement in cyclic plasticity modeling for multiaxial ratcheting simulation. *International Journal of Plasticity*, 18(7):873–894, July 2002. doi: 10.1016/S0749-6419(01)00012-2.

[110] K. A. Meyer, R. Skrypnyk, and M. Pletz. Efficient 3D finite element modeling of cyclic elasto-plastic rolling contact. *Tribology International*, 161:107053, September 2021. doi: 10.1016/j.triboint.2021.107053.

[111] J. A. Cuadra, P.A. Vanniamparambil, D. Servansky, I. Bartoli, and A. Kontsos. Acoustic emission source modeling using a data-driven approach. *Journal of Sound and Vibration*, 341:222–236, April 2015. doi: 10.1016/j.jsv.2014.12.021.

[112] J. A. Cuadra, K. P. Baxevanakis, M. Mazzotti, I. Bartoli, and A. Kontsos. Energy dissipation via acoustic emission in ductile crack initiation. *International Journal of Fracture*, 199(1):89–104, February 2016. doi: 10.1007/s10704-016-0096-8.

[113] M. G. R. Sause and S. Richler. Finite element modelling of cracks as acoustic emission sources. *Journal of Nondestructive Evaluation*, 34 (1):1–13, February 2015. doi: 10.1007/s10921-015-0278-8.

[114] A. Uhnáková, A. Machová, P. Hora, J. Červ, and T. Kroupa. Stress wave radiation from the cleavage crack extension in 3D BCC iron crystals. *Computational materials science*, 50(2):678–685, October 2010. doi: 10.1016/j.commatsci.2010.09.033.

[115] P. Hora, O. Červená, A. Uhnáková, A. Machová, and V. Pelikán. Stress wave radiation from brittle crack extension by molecular dynamics and FEM. *Applied and Computational Mechanics*, 7(1):23–30, June 2013.

[116] B. Poddar and V. Giurgiutiu. Detectability of crack lengths from acoustic emissions using physics of wave propagation in plate structures. *Journal of nondestructive evaluation*, 36(2):1–13, May 2017. doi: 10.1007/s10921-017-0392-x.

[117] W. Döll. Kinetics of crack tip craze zone before and during fracture. *Polymer engineering and science*, 24(10):798–808, July 1984. doi: 10.1002/pen.760241009.

[118] W. H. Prosser, M. A. Hamstad, J. Gary, and A. O'Gallagher. Finite element and plate theory modeling of acoustic emission waveforms. *Journal of nondestructive evaluation*, 18(3):83–90, September 1999. doi: 10.1023/A:1021888009896.

[119] J. C. Yeh and C. L. Tsai. Study of acoustic emisison characteristics for fracture assessment. *Review of Progress in Quantitative Nondestructive Evaluation*, 12(1):2207–2213, January 1993. doi: 10.1007/978-1-4615-2848-7_283.

[120] A. Rohatgi. Webplotdigitizer: Version 4.5, 2021. URL `https://automeris.io/WebPlotDigitizer`. [Online; accessed May-2022].

[121] A. F. Bower. *Applied mechanics of solids*. CRC Press, Florida, 2010.

[122] A. Posmyk H. Bakowski and J. Krawczyk. Tribological properties of rail steel in straight moderately loaded sections of railway tracks. *Archives of metallurgy and materials*, 56(3):813–822, September 2011. doi: 10.2478/v10172-011-0090-0.

[123] F. J. Franklin, J. Garnham, D. I. Fletcher, C. Davis, and A. Kapoor. Modelling rail steel microstructure and its effect on crack initiation. *Wear*, 265(9):1332–1341, October 2008. doi: 10.1016/j.wear.2008.03.027.

[124] G. R. Johnson and W. H. Cook. A constitutive model and data for metals subjected to large strains high strain rates and high temperatures. *In Proceedings of the Seventh International Symposium on Ballistics*, 21:541–548, April 1983.

[125] S.K. Maitii. *Fracture mechanics: Fundamentals and applications*. Cambridge University Press, Delhi, India, 2015.